RESEARCH ARTICLE

A Fast Level-Set Curve-Flow Formulation by Logarithmic Step-Size Control for Brain Ultrasound Image Segmentation

HARADHAN CHEL[1], **(Member, IEEE), PRABIN KUMAR BORA**[2],
AND KANDARPA KUMAR RAMCHIARY[3], **(Member, IEEE)**

[1]Department of Electronics and Communication, Central Institute of Technology Kokrajhar, Kokrajhar, Assam 783370, India
[2]Department of Electronics and Electrical Engineering, Indian Institute of Technology Guwahati, Guwahati 781039, Assam, India
[3]Department of Radiology, City Clinic and Research Centre, Kokrajhar 783370, Assam, India

Corresponding author: Haradhan Chel (h.chel@cit.ac.in)

ABSTRACT Segmentation of different regions in intra-operative brain ultrasound (iBUS) images is often required for assisting the neuro-surgeon. Traditional level-set and active contour-based semi-automatic image segmentation approaches suffer from low accuracy and slow convergence. This paper presents a novel semi-automatic level-set approach for segmenting hyper-echoic (HE), hypo-echoic, and anechoic regions with minimal user intervention. Three HE regions *longitudinal fissure, choroid plexus, and tumor* and two anechoic regions, namely *ventricle and resection cavity* are segmented using a patch-based level-set approach. This method is a combination of three procedures: a) *unidirectional level-set curve flow* (ULSCF), b) *bidirectional level-set curve flow* (BLSCF) using a logarithmic patch size control, and c) cubic B-spline-based *contour smoothing*. The zero level-set curve is derived using a patch-based intensity thresholding method of the desired region. The imperfection on the blocky edges produced during the patch-based ULSCF, are minimized using the BLSCF step that uses a local region splitting approach. Slope and curvature discontinuities of the resulting boundaries after BLSCF are eliminated using cubic B-spline based contour smoothing. The proposed method outperforms other state-of-the-art level-set and active contour methods, and the desired result is obtained within reasonable time required for online monitoring during surgery.

INDEX TERMS Ultrasound guided surgery, ultrasound image segmentation, patch-based segmentation, boundary correction, contour smoothing.

I. INTRODUCTION

The segmentation of ultrasound(US) images is important in the diagnosis of various tissue abnormalities, detection of the shape and size, and the state of the diseased region. Its applications include segmenting the fetus [1], [2], [3], the prostate [4], kidneys [5], blood vessels [6], [7], [8], etc. Segmenting a US image is a challenging task because of its poor resolution, the presence of speckle, acoustic shadows, and unnatural scattering due to the presence of blood clotting agents in the surgical cavity [9], [10]. Traditional segmentation methods [11] like region growing, region splitting, morphological segmentation, etc. do not

perform well for the US image segmentation due to the intensity inhomogeneity in the images. The state-of-the-art approaches to the segmentation of US images include Markov random field (MRF) modelling [12], watershed based segmentation [13], level-set [14], [15], [16], [17], [18], [19], [20], [21], machine learning (ML) [22], [23], [24], and deep learning(DL) [25], [26], [27], [28], [29], [30], [31], [32], [33].

This article primarily focuses on the segmentation of brain US (BUS) images as a prework to the brain image registration. Brain surgery is generally performed with the assistance of a neuro-navigation(NN) system that consists of both pre-operative and intra-operative imaging facilities. Intra-operative magnetic resonance(iBMR) is generally preferred compared to the intra-operative ultrasound(iBUS) for

The associate editor coordinating the review of this manuscript and approving it for publication was Joewono Widjaja.

its better resolution and visibility of different regions. The iBMR is not real-time and it has a large infrastructural cost that limits its use to large super-specialty hospitals only. Intra-operative brain computed tomography (iBCT) imaging is a low-cost alternative to iBMR, but it has the harmful ionization effect on the human body. US has limited applications in brain imaging because of its inability to propagate through bones. After opening the cranial bone during the surgery, US can be used as an intra-operative modality to examine the brain tissues. Therefore, pre-operative BUS (pBUS) and iBUS can be used in an NN system to monitor the diseased tissues during the brain surgery. In US-guided brain surgery, the pBUS and iBUS images are rendered side by side. To monitor the surgical process in real-time, the location of the surgical equipment inside the brain is precisely mapped on the rendered pre-operative image stacks. It is performed using the following two steps [34]:

1) Before surgery, the NN system is calibrated with the brain coordinate system using fiducial markers placed on some predefined locations of the patient's head. This calibration pinpoints the position of the surgical instrument inside the brain, and shows it on the pBUS image stacks on the computer screen. No image related data are required for this calibration.

2) After opening the brain and before opening the dura mater, pBUS images can be captured using a suitable US probe. These images show the latest position of the diseased region without any spatial shift or any shape distortion. The brain is composed of soft tissues that floats in cerebrospinal fluid (CSF). Brain-shift is a common phenomenon that occurs during the surgical procedure. It happens due to various reasons like applied pressure, leakage of CSF, edema, act of gravitation, etc. [35]. Because of the brain-shift, the NN system lose its calibration to the previously aligned image stacks. Therefore, the location of the diseased region in a iBUS image does not match to the corresponding location in the pBUS image. Unless the system is registered, the position of the surgical equipment maps into a wrong position in the pre-operative image stack. An efficient registration method is therefore essential between the shifted iBUS and pBUS images to bring back the calibration of the NN system.

The registration between pBUS-iBUS images is challenging due to poor resolution, low visibility, and presence of various artifacts. For the effective registration between pBUS and iBUS images, common regions should be present in the registering image pairs. iBUS images suffer from various artifacts due to the presence of saline water in the resection cavity (RC), acoustic shadows, scattering, etc. As a result, the desired level of similarity cannot be guaranteed. Brain image segmentation is an effective prework for improving the similarity between the pBUS and the iBUS images [24], [33], [36]. It can isolate the similar regions from the pBUS and iBUS images.

Based on the echogenicity, the regions of a B-mode BUS image can be classified into *hyper-echoic, hypo-echoic*, and *anechoic* regions [37]. The regions producing large echos, appear bright and are known as HE. In a BUS image, the *choroid plexus* (CP), *tumors* (third or higher grade), *longitudinal fissure* (LF), and *corpus callosum* (CC) [10] appear HE. The regions which mostly contain fluids and do not produce large echos, thus appearing black are known as anechoic regions. All four *ventricles*, *sub-arachnoid space, blood vessels*, and *cyst* appear anechoic. Other regions with moderate echogenicity like *thalamus*, *caudate nucleus*, and *cerebrum* are seen as hypo-echoic regions.

Level-set is a curve evolution strategy that was first formulated by Osher and Sethian [38]. Application of the classical level-set includes evolving interfaces in computation geometry, fluid mechanics, material science, and computer vision and image processing [39]. It consists of two major steps: a) Energy function formulation and b) Level-set curve evolution. There are various approaches to the level-set, such as geodesic active contour (GAC) [14], active contour without edge (ACWE) [17] and distance regularized level set evolution (DRLSE) [20]. For the segmentation of speckle-free images, the performance of these methods is satisfactory; however, when speckle increases, it degrades significantly. Figure 1 depicts these occurrences, with segmented outputs from the GAC, ACWE, and DRLSE on speckle-free images (a1), (b1), and (c1) respectively. The segmented outputs are shown by the red-colored boundaries. Five zones contain different intensities with different intensity gradients on the boundaries. The increase in the intensity gradient makes the segmentation easy. Out of 5 different shapes, the pentagonal region have the least intensity gradient. All three algorithms successfully segment all the five zones in the absence of speckle. However, as the speckle variance increases, their performance degrades. The output for a speckle variance of 0.01 is shown in Figure 1.(a2), (b2), and (c2), and the output for a speckle variance of 0.1 is shown in Figure 1.(a3), (b3), and (c3) respectively. The speckle used in these images is synthetic and was developed in MATLAB using the methodology outlined in [2]. The hexagonal region has stronger intensity gradients than other boundaries, which were segmented using the ACWE approach, but failed by DRLSE and GAC. The segmentation of the pentagonal region fails for all these methods for a speckle variance of 0.01 and higher, which are shown in (a2-c2) and (a3-c3). Based on these findings, we conclude that the level-set-based approaches are significantly influenced by speckle. Our suggested solution uses a patch-based level-set-based architecture that is fast, speckle-resistant, and yields adequate accuracy. Our proposed approach is topology-independent and produces regular-shaped boundaries of the desired regions.

Recently, ML- and DL-based approaches are being used widely for medical image segmentation. DL-based segmentation methods have been successfully applied for the segmentation of the prostate [23], [40], [41], ovary and
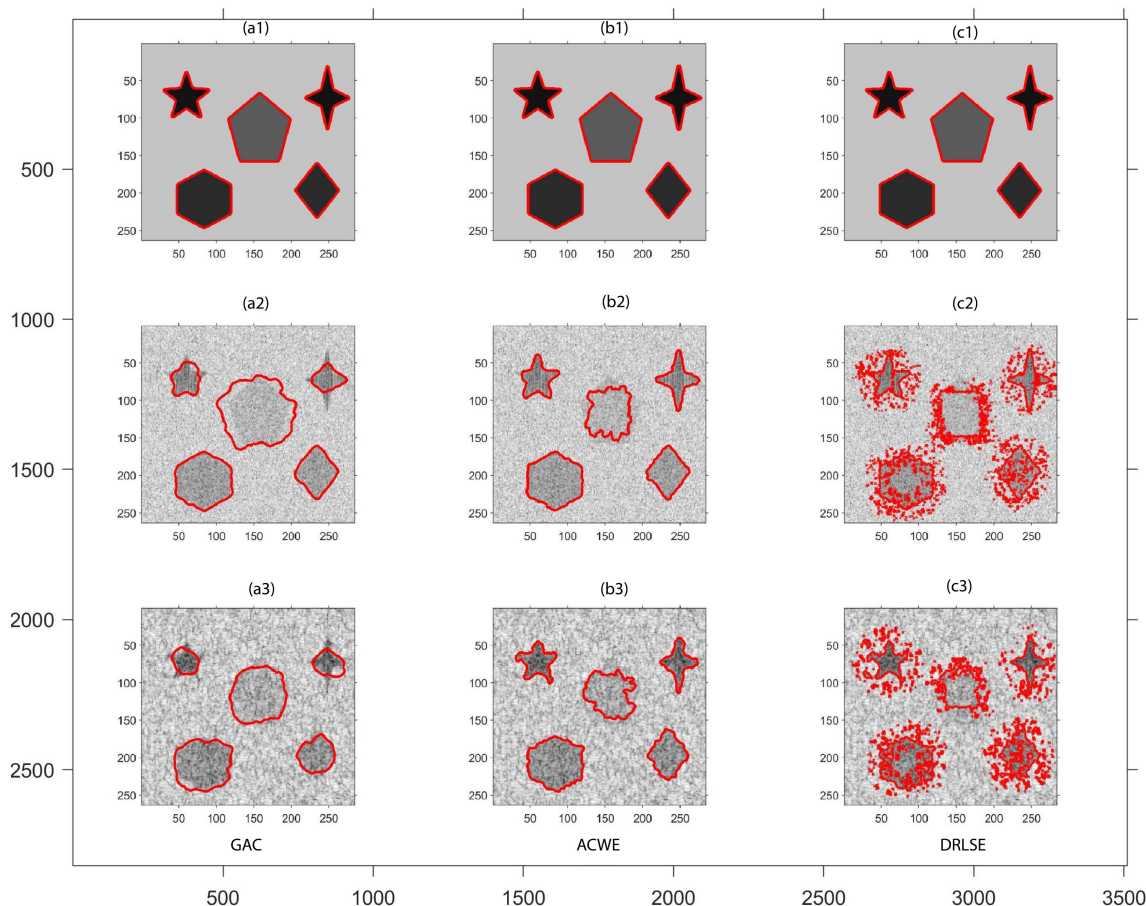
FIGURE 1. (a1), (b1), and (c1) are specklefree phantom images. The results of the various segmentation algorithms are represented by red boundaries across these images. The GAC method's outputs are (a1) to (a3), the ACWE method's outputs are (b1) to (b3), and the DRLSE method's outputs are (c1) to (c3). The outputs for the speckle of variance 0.01 are shown in rows (a2)-(c2), while the outputs for the speckle of variance 0.1 are shown in rows (a3)-(c3).

its follicles [26], thyroid nodule [42], optic nerves [43], breast tumors [28], [29], [30], kidneys [44], [45], arteries [32], heart [46], [47], fetus [48], [49], [50], intracranial aneurysms [51], etc. The successful architectures applied in this field are U-Net [42], [46], [52], CR-Unet [26], 3D ResNet [40], [53], Dual Path U-Net (DPU-Net) [31], Dense-Net [32] and the generative adversarial network (GAN) [28]. Most of these models are fully supervised learning-based. They require radiologists to annotate large-scale training data, which is rather a labour-intensive and time-consuming task. To alleviate this issue, many researchers attempted implementing segmentation tasks in a semi-supervised manner using limited annotated images [54], [55]. Meng et al. [48] followed a semi-supervised approach to find the acoustic shadow in fetal US images. To the best of our knowledge, there are no big labeled datasets available for 2D BUS image segmentation.

In a patch-based segmentation of BUS image [56], we introduced a fully automatic patch-based method for extracting the HE regions from the pBUS and iBUS images. Generally, the HE regions possess better similarity between the pBUS and iBUS images. But many image pairs have smaller HE regions between them. The extraction of those regions cannot attain much similarity between the registering image pairs and the registration often fails. On the other hand, many anechoic and hypo-echoic regions present in the pBUS and the iBUS images also contain significant information that may help in registration. The inclusion of the anechoic and the hypo-echoic regions, improves the accuracy of the estimation of the transformation function. This article focuses on the segmentation of five specific regions with different levels of echogenicity. It is a semi-automatic approach that requires minimal user intervention to mark the desired region for segmentation.

A. EXISTING METHODS FOR BUS IMAGE SEGMENTATION

Literature on BUS segmentation is limited to a few recent publications only. Canalini et al. [33] extracted various HE regions as a preprocessing step for the registration between pBUS and iBUS images. Nitsch et al. [24] used a superpixel-based approach. This method applied a random forest-based classifier for segmenting various regions of the BUS and MR images. The ML model trained with random-forest algorithm, finds the posterior probabilities of a

superpixels to be in a segment. For obtaining a segment, concatenation of multiple sub-clusters are performed applying various rule-based thresholding of the posterior probabilities. Chel et al. [56] published an automatic patch-based approach for the separation of HE regions from the BUS images. It is simple and uses thresholding, morphological hole filling, and B-spline curve shaping for obtaining the accurate boundaries of different HE regions.

The proposed method is an extension of the method in [56]. It contributes the following novel features to the previous method.

- Five different regions namely the LF, CP, tumor, ventricles, and RC are segmented using a common segmentation framework. The segmentation can be performed irrespective of their grades of echogenicity.
- It automatically detects the region types, and estimates the thresholds for the segmentation of the desired regions. Like its predecessors, the proposed method is topology-independent and results in regular-shaped boundaries between different echogenic regions.
- It adopts a level-set based framework that is fast, immune to speckle, and results in an acceptable accuracy. The previous method was only capable of separating the HE regions from the BUS images. This method can automatically segment all three types of echogenic regions.

B. LEVEL-SET FORMULATION FOR IMAGE SEGMENTATION

The iterative growth of the boundary curve is modeled by an implicit level-set geometry. It defines the boundary as a level-set function $\phi(x, y) = 0$, whereas $\phi(x, y) > 0$ and $\phi(x, y) < 0$ represent the inside and the outside regions respectively. $\phi(x, y)$ is a distance function which defines the distance of (x, y) from $\phi = 0$. The normal vector $\mathbf{n}$ and the curvature (κ) of the $\phi = 0$ curve can be expressed as,

$$\mathbf{n} = \frac{\nabla\phi}{|\nabla\phi|} \tag{1}$$

and,

$$\kappa = \nabla.\frac{\nabla\phi}{|\nabla\phi|} = \frac{\phi_{xx}\phi_y^2 - 2\phi_x\phi_y\phi_{xy} + \phi_{yy}\phi_x^2}{\left(\phi_x^2 + \phi_y^2\right)^{\frac{3}{2}}} \tag{2}$$

Let $\phi(t, x, y)$ be the state of the curve at time t, and the velocity of the curve along the normal direction be $v = F\mathbf{n}$, where F is a scalar quantity named as *force*. $\phi(t, x, y)$ is obtained by the solution of the following partial differential equation (PDE):

$$\frac{\partial\phi(t, x, y)}{\partial t} + F\nabla^T\phi(t, x, y)\mathbf{n} = 0 \tag{3}$$

Upon substituting (1), we get

$$\frac{\phi(t, x, y)}{\partial t} + F|\nabla\phi(t, x, y)| = 0 \tag{4}$$

which explains the temporal evolution of ϕ.

In the above formulation, the first term states about the change of ϕ over time, that describes about the spatial shift of zero level-set curve. The solution of this PDE in every iteration is computationally intensive, that restricts its application in real time. For a constant value of F, the zero level-set curve moves uniformly on the normal direction. However, for image segmentation, F is made image dependent so that the growth of the curve depends on the image intensity profile and its shape. Several variations of level-set-based image segmentation are found in literature, such as ACWE [17], DRLSE [20], variational B-Spline Level-Set [18], and the recent works like weighted level-set evolution (WLSE) [57]. All these approaches are extensively used for US image segmentation. Solution of the PDE in (4) in every iteration is computationally expensive due to energy estimation of the whole image. For reducing the computational complexity, Bernard et al. [18] estimated energy in the neighborhood of the evolving curve; thus it reduces the complexity. For maintaining the numerical stability in the PDE solution process, small time steps are chosen. The level-set function and a narrow band surrounding to the zero-level-set curve must be updated in each iteration. This concept significantly speeds up the curve evolution process. Shi and Karl [19] also applied the concept of energy estimation in the neighborhood but it does not apply the solution of the PDE. In place of that, it adopts two procedures for curve movement along the inward or outward directions.

Even after so many efforts, the noise plays a crucial role for the segmentation by adding ambiguity on the boundaries. Many times, false edges prematurely stop the curve evolution and add shape distortion to the boundaries. To address these limitations, this paper proposes a novel segmentation algorithm that retains key advantages of the level-set approach in a practical and highly efficient manner. It considers a square patch in place of a pixel in traditional level-set function, which reduces the effect of noise and computation time. It reduces the computational burden for estimating the curvature and avoids the complexity for the solution to the PDE.

C. PATCH-BASED LEVEL-SET CURVE FLOW

In a patch-based approach, the image region $\Omega \epsilon \mathbb{R}^2$ is assumed to be a grid of patches of size $w \times w$. The movement of the level-set curve flows over the vertical and the horizontal direction. There is no movement of the curve in a region of the size less than $w \times w$. For numerical stability, the growth of ϕ is limited to 1 unit only. Figure 2 illustrates the proposed level-set framework. The region bounded by red-colored contour is the desired region to be segmented. The ROI of the desired region is marked by a rectangular region $\mathbf{R}$ shown by a black colored boundary. The boundary line made of green dots represents the $\phi = 0$ curve or C_0. ϕ is a 2D Signum function which makes the transition at $\phi = 0$ boundary. The region inside C_0 has $\phi = 1$ and $\phi = -1$ outside. C_0 is the initial state of the level-set curve evolution. The detailed method of
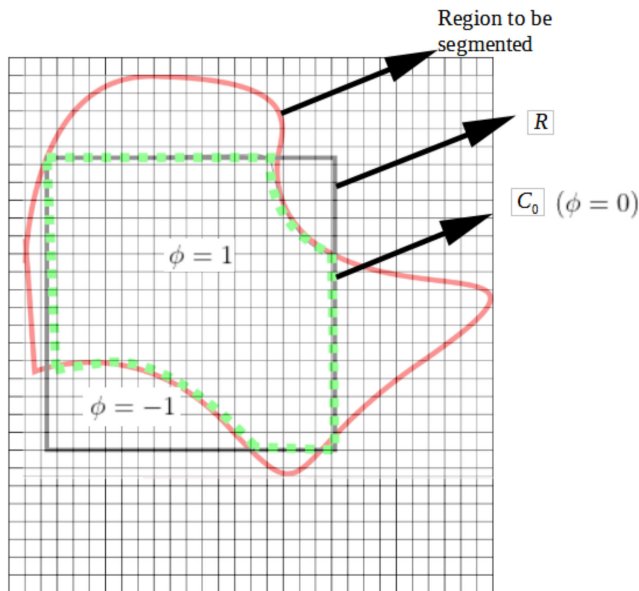
FIGURE 2. Representation of the level-set function ϕ in patch-based scenario.

FIGURE 3. Proposed level-set framework.

obtaining C_0 and its evolution are described in Section (II-B) and (II-C) respectively.

II. PROPOSED METHOD

The statistical nature of the intensity profile of a segmenting region is not taken into account by the existing approaches to level-set-based image segmentation. Anechoic, hypo-echoic, and HE regions in BUS images have distinct statistical properties. Hence, a technique that effectively segments an anechoic region may not work for a HE region. The proposed approach takes the advantage of local statistics and offers a strategy that works equally well in all three kinds of regions. The level-set-based image segmentation framework serves as the foundation for the proposed work. Its complexity is avoided by excluding the energy minimization step. This step is substituted by simple patch-based intensity thresholding in the proposed methodology. Three main issues are addressed:

- stop curve evolution at the boundary
- avoid boundary ambiguities caused by speckle
- obtain a smooth boundary curve that does not have slope and curvature discontinuities

As discussed earlier, the spatial curve gradient, whose magnitude depends on the image intensity profile, determines the direction of the iterative growth of the initial level-set curves. The boundaries of speckle-filled images are uneven and as a result, the movement in the normal direction causes segmented boundary to become more distorted. To prevent this, the curve's length and the area of the bounded region are added to the energy function as regularization parameters [17], [19], [20], [57]. The proposed method does not apply energy optimization, but it applies a contour smoothing step to find a smooth boundary of the segmenting regions
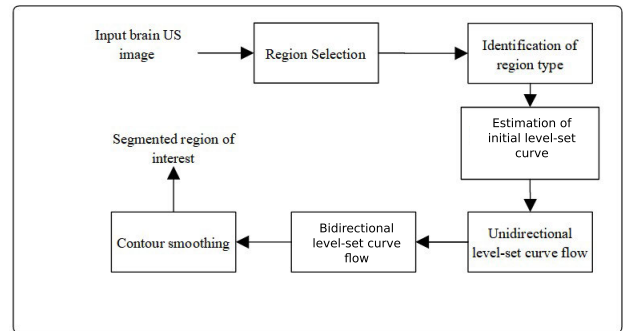
The work-flow of the proposed method is shown in Figure 3. Averaging of intensity within a square patch reduces the speckle variance. The proposed method adopts patch-based thresholding in various steps. At the start of the segmentation process, the user selects one or more rectangular regions within the region of interest(ROI) denoted by Ω_R. The selection is made in such a way that Ω_R contains only one type of echogenic region. The region type of Ω_R is identified by using a thresholding method as described in Section II-A. The next step applies a patch-based thresholding of Ω_R.

The statistical natures of three types of echogenic regions are different, and therefore, they need different formulations for the estimation of region specific threshold ranges. The region Ω_R is divided into non-overlapping square patches. If the mean intensity of a patch is within T_l and T_h, it is included in the *inside* region and excluded otherwise. The formulation of T_l and T_h for three different types of echogenic regions are described in Section II-A1. The first step of the level-set curve evolution is the estimation of initial level-set curve $\phi(0, x, y)$. This step is described in Section II-B. Section II-C describes how $\phi(0, x, y)$ expands over time by a patch-based unidirectional level-set curve flow (ULSCF) step. This step results in a gross segmentation of the region. However, the boundaries suffer from blockiness due to patch-based processing. The larger is the size of the patches, the higher is the blockiness. The bidirectional level-set curve flow (BLSCF) step adopts a patch-based bidirectional level-set evolution that increases the proximity of the resulting boundaries to the actual boundaries as described in Section II-D. The resulting boundary after BLSCF, suffers from slope and curvature discontinuities, which is rectified by a contour correction step which is described in Section II-E.

A. IDENTIFICATION OF REGION-TYPE

For minimal user intervention, automatic identification of the region type is necessary. Three different types of regions can be identified by the statistics of the intensity profile of a region. First, we find a range of the mean intensity of the region. For ascertaining the range of mean intensities of different types of regions, one or multiple rectangular sections
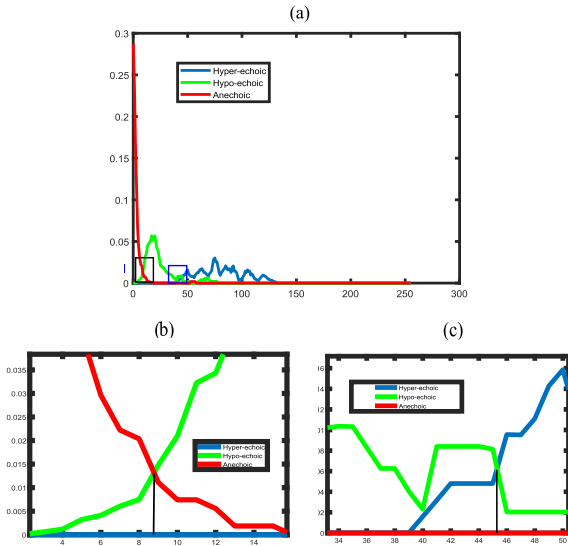
FIGURE 4. (a) Intensity histogram of the three different echogenic regions. Colored boxes highlight the intersection between different histograms. (b) is the enlarged box that highlights the intersection between the anechoic and the hypo-echoic histograms. (c) is the enlarged box that highlights the intersection of the HE and the hypo-echoic histograms.

are marked from the HE, the hypo-echoic, and the anechoic regions of randomly selected 160 images from the BITE [10] and the RESECT [58] datasets. The mean intensity (μ_R) of the chosen rectangular regions Ω_R is obtained by

$$\mu_R = \frac{1}{|\Omega_R|} \sum_{(x,y) \in \Omega_R} I(x, y) \qquad (5)$$

where $|\Omega_R|$ is the number of pixels in Ω_R.

Ω_R is chosen in such a way that it covers the maximum possible area of a region. Marking of the rectangular region is flexible and it is made in such a manner that its average intensity is close to the actual average intensity of the desired segment. The μ_R values for each types are plotted in a normalized histogram as shown in Figure 4.

We observed that for an 8-bit image, the mean intensity lies between 0-15 for an anechoic region, between 4-75 for a hypo-echoic region, and between 45-150 for an HE region. The types of regions are decided by comparing the average intensity (μ_R) of the user-defined ROI to the said ranges of intensities. The intersection points of different histograms are obtained using the maximum likelihood principle. Figure 4.(b) highlights the intersection between anechoic and hypo-echoic regions and it was found that both the histograms intersect at 8.2. Thus, we set a threshold value of 8.2 between the anechoic and the hypo-echoic regions, whereas 45.6 is set between hypo-echoic and HE regions. Hence, if $\mu_R \leq 8.2$, the region can be treated as anechoic. Similarly, if $8.2 \leq \mu_R \leq 45.6$, it is hypo-echoic, else it is HE.

The proposed method adopts a patch-based level-set strategy for the segmentation of the desired region. The user-selected region Ω_R partially includes the desired region. The part of Ω_R that consists of the desired region is defined as the inside region and the rest of the part is termed as the

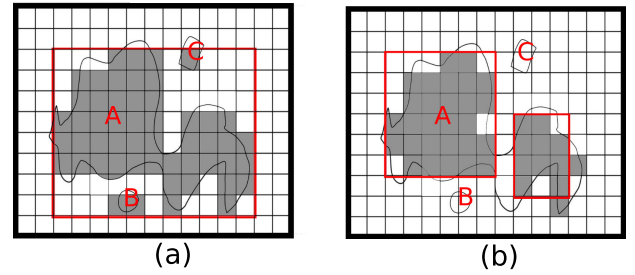**FIGURE 5.** Ω_R is the ROI, marked in red color. In (a), the ROI encompasses multiple objects. In (b), the ROI is the combination of the two rectangles.

outside region. The segmentation growth of the desired region starts from the initial level-state-curve. This step divides Ω_R into multiple square patches of size $w \times w$. Depending on the region type, two thresholds are estimated based on the statistical nature of Ω_R. The estimation of T_l and T_h is described in Section II-A1.

1) ESTIMATION OF T_H AND T_L

Once the region-type is identified, the pixels in Ω_R are to be associated with the inside or the outside the desired region. This association is done patch-wise by comparing the average patch intensity with two thresholds T_l and T_h. These thresholds are used for the patch-wise association of the pixels to the desired region in a level-set-based formulation. Ni black proposed a local patch-based threshold scheme which combines the mean and standard deviation of intensity of a local patch [56], [59]. Noting that the standard deviation controls the spread of the data, we formulate the T_l and T_h as

$$T_l = \mu_R - k_1 \sigma_R \qquad (6)$$
$$T_h = \mu_R + k_2 \sigma_R \qquad (7)$$

where σ_R is the standard deviation of the image in Ω_R and k_1 and k_2 are constants. The values of k_1 and k_2 for different region types are determined by the trial and error method and thus, T_l and T_h are formulated as follows:

1) *Anechoic region*

$$T_l = 0$$
$$T_h = \mu_R + 0.5\sigma_R \qquad (8)$$

2) *Hypo-echoic region*

$$T_l = max(0, \mu_R - \sigma_R)$$
$$T_h = min(255, \mu_R + 1.5\sigma_R) \qquad (9)$$

3) *Hyper-echoic region*

$$T_l = max(0, \mu_R - 0.5\sigma_R)$$
$$T_h = min(255, \mu_R + 1.5\sigma_R) \qquad (10)$$

The *max* and *min* terms in (9) and (10) are used to limit the values of T_h and T_l within the dynamic range of intensity 0-255 for 8 bit images. Both T_l and T_h have an important role in determining C_0 and estimating $\phi(n, x, y)$ as described in Sections II-B and II-C respectively.

B. ESTIMATION OF INITIAL LEVEL-SET CURVE

Let an input image I be defined on the domain Ω and $\Omega_R \subseteq \Omega$ be the initial rectangular region of size $M \times N$ chosen by the user. Let Ω_R be divided into non-overlapping square patches $P(i, j) : 1 \leq i \leq K$ and $1 \leq j \leq L$ of size $w \times w$. The value of w is an integer power of 2 like 4, 8, 16, etc. Large value of w decreases the computation time but increases the boundary error. Similarly, the small values of w increases computation time, and number of sub regions within a region, but improves the boundary errors. Keeping these in mind, $w = 8$ was found optimum for images of both the BITE and the RESECT datasets. The region Ω_R is extended so that M and N are integer multiples of the patch size $w \times w$. The mean intensity of $P(i, j)$ is given by

$$\mu(i, j) = \frac{\sum \sum_{(x,y) \in P(i,j)} I(x, y)}{w^2} \qquad (11)$$

$\mu(i, j)$ is compared with T_l and T_h. If $T_l \leq \mu(i, j) \leq T_h$, $P(i, j)$ is considered as *inside* patch and included in Ω^{inside}. Hence, the inside region extracted from Ω_R can be expressed as,

$$\Omega^{inside} = \bigcup_{\forall(i,j):T_l \leq \mu(i,j) \leq T_h} P(i, j) \qquad (12)$$

The boundary of the region Ω^{inside} is the initial level-set curve C_0. We define a level-set function $\phi(n, x, y)$ as follows.

$$\phi(n, x, y) = \begin{cases} = 1 & (x, y) \in \Omega^{inside} \\ = -1 & (x, y) \in \Omega^{outside} \end{cases} \qquad (13)$$

We define the level-set function as the interface between $\phi(n, x, y) = 1$ and $\phi(n, x, y) = -1$ regions. In Figure 5, the gray patches satisfy the threshold condition. The boundary of this region represents C_0 encompasses a part of the desired segmenting region. For segmenting a region with a complex shape, multiple rectangles can also be marked. Overlapping between these rectangles is also allowed during this step. The number of regions and their sizes play important roles in overall speed of the segmentation. A large rectangular region may include many undesired small regions and corresponding μ and σ also change compared to the actual value of the region. It may results into an ineffective segmentation. On the other hand, choosing multiple rectangles increases the user intervention. For example, Figure 5.(b) shows two rectangular regions and the ϕ map of the region. The same segmentation can be performed with any one rectangle also. But it takes more iterations during the level-set curve flow; thus overall complexity increases.

C. UNIDIRECTIONAL LEVEL-SET CURVE FLOW (ULSCF)

As discussed in Section II-B, all the pixels in a $w \times w$ patch have the same value of ϕ, and thus are expressed patch-wise. Let $\phi(n, i, j)$ be the level-set function value of $(i, j)^{th}$ patch at iteration n. The patch $P(i, j)$ is given by $P(i, j) = \{(x, y) | (i - 1)w \leq x \leq (i + 1)w - 1 \text{ and } (j - 1)w \leq y \leq (j + 1)w - 1\}$. In the proposed method, $\phi(0, i, j)$ is obtained by threshold estimation and comparison

method as described in Section II-B. The initial level-set curve flow starts from $\phi(0, i, j)$ and it moves toward the outward direction from C_0. This step is iterative and in every iteration, the boundary moves to the outward directions. Suppose C_k is the boundary at k^{th} iteration. A one patch wide neighborhood N_k is defined in the outside region of C_k. If a patch in N_k satisfies the condition $T_l \leq \mu(i, j) \leq T_h$, its ϕ value changes from -1 to +1 and the patch is included in the inside region. It is similar to the pixel-based flow in [19], that drives the boundary in the outward direction. Unlike the method in [19], the flow in this step is allowed to one patch outward per iteration from C_k. This movement is allowed to the outward neighbouring patches of C_k. This approach is faster because of the bigger movement of the boundaries. Secondly, the pixel-based method is not immune to noise and produces ambiguous boundaries. Patch-wise averaging has a smoothing effect and is robust to noise. The flow of the level-set function values over time can be expressed as

$$\phi(n + 1, i, j)$$
$$= \phi(n, i, j) + 2 \underbrace{H(\mu(i, j) - T_l)H(T_h - \mu(i, j))}_{forcefunction}$$
$$\forall(i, j) \in N_n \qquad (14)$$

where $H(.)$ is the Heavieside function. The change in the value of ϕ depends on a force function. The force function is a Heavieside function which results unity when a patch satisfies the threshold condition. The level-set curve flow is comparatively faster at a homogeneous region and becomes slow when approaching the boundary of the level-set curve [19]. The flow in the proposed method is uniform and with a larger step size. Figure 6.(a) shows the growth of ϕ during this step by cyan color. It takes mostly seven iterations to reach to the boundary of the desired region. If 2 rectangles marked by red colored boundaries are considered in the beginning as shown in Figure 5.(b), the same region can be covered within one iteration only. It describes about the flexibility in ROI selection, that can reduce the execution time. Like other conventional level-set methods, this method can join multiple growing regions during this step. It can also split from the initial ROI to multiple regions during initialization of ϕ_0. These properties make this method topology-independent.

The evolution of the $\phi = 0$ is continued until there is no change in the ϕ. In other words, iteration continues until $\sum_{\forall(i,j)} |\phi(n, i, j) - \phi(n - 1, i, j)| = 0$.

D. BIDIRECTIONAL LEVEL-SET CURVE FLOW (BLSCF)

For obtaining smooth boundaries, other level-set methods add the curvature to the energy function as a regularization term [17], [19], [20], [57]. These methods require extra calculations in every iteration for the estimation of the curvature of C_k. We obtain curve smoothness in a simple and fast manner. The ULSCF described in the previous subsection performs patch-wise segmentation in the selected region and results in block-like boundaries. Let the stopping criteria be
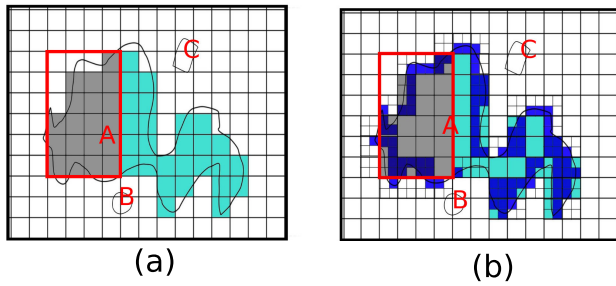
FIGURE 6. (a) ULSCF starts from the boundary of the gray region. The *cyan* region of ϕ is grown during ULSCF. (b) During BLSCF, each patch connected to C_0 is divided into 4 equal-sized square sub-patches. If a sub-patch maintains the prescribed threshold condition is retained/added to $\phi = 1$ region; otherwise, $\phi = -1$. This modification is shown in blue color.
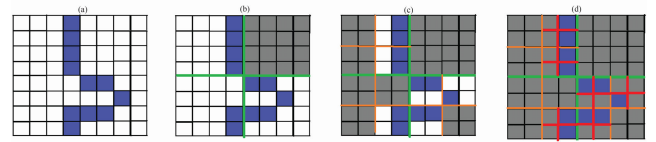

FIGURE 7. (a) Shows a 8 × 8 boundary patch after ULSCF. The connected blue-coloured pixels show the one-pixel wide actual boundary. A gray sub-patch indicates that there is no boundary pixel within it. (b) shows the top right 4 × 4 sub-patch does not main threshold condition and turned gray. (c) shows the resulting boundary with a patch size of 2 × 2, and (d) the final boundary is obtained after boundary correction with patch size 1 × 1.

met after J iterations and it produces a blocky boundary C_J. To reduce the blockiness of the obtained boundary, both the inside and the outside patches connected to C_J are needed to be observed closely on a finer scale. Figure 6.(a) shows the graphical representation of $\phi(J, i, j)$ after the ULSCF for a patch size of $w \times w$. Here the gray patches represent the initial inside region. Before starting the level-set curve flow, both white and cyan patches remain in the outside region. Out of those patches, the cyan patches are within the desired region which is needed to be labeled as inside, and the white patches are needed to be labeled as outside patches.

In this step, C_J obtained in the ULSCF step is reinitialized as C_0, which is an approximate shape to the desired boundary. The neighbourhood of C_0 is also redefined as N_0, which is the union of both inside and outside patches connected to C_0. Unlike the ULSCF, both inward and outward movement is allowed in this step. It is an iterative process for of $log_2(w)$ iterations. In each iteration, the value of w is made half of the value of it in the previous iteration. Therefore, after $log_2(w)$ iterations $w = 1$, which turns into pixel-based processing. The following steps are performed in each iteration

1: **while** $w > 1$ **do**
2:     set k=0
3:     Determine the bidirectional neighborhood N_k of C_k. C_k is the union of the 8-connected patches of size $w \times w$. First, all patches having a transition of ϕ from -1 to +1 or vice versa and sharing at least one side with C_k, are identified. For each of these patches, the bidirectional neighborhoods are included in N_k.
4:     Divide each $w \times w$ patch $P(i, j)$ in N_k that are connected to C_k into four sub-patches of size $\frac{w}{2} \times \frac{w}{2}$. Assign each sub-patch with the ϕ value of the $w \times w$ patch. Update the values of $\phi(k, i, j)$ as follows
5:     Set $w = \frac{w}{2}$
6:     Compute $\mu(i, j)$ using (11)
7:     **if** $\phi(k, i, j) = 1$ **then**
8:

$$\phi(k, i, j) = \phi(k, i, j) \\ - 2\left[1 - H(\mu(i, j) - T_l)H(T_h - \mu(i, j))\right]$$

9:     **else** $\phi(k+1, i, j) = \phi(k, i, j) + 2H(\mu(i, j) - T_l)H(T_h - \mu(i, j))$
10:     **end if**
11:     $k \leftarrow k + 1$
12: **end while**

Figure 6.(b) shows the modification to the existing boundary patches shown by blue colors. All the blue-colored patches satisfy the threshold conditions and are included in the inside region. Similarly, if a sub-patch does not satisfy the threshold condition, $\phi(k, i, j)$ becomes -1.

The boundary generated by the ULSCF was $w \times w$, which indicated poor resolution at the boundary. The actual boundary remains hidden within this patch of $w \times w$. During BLSCF, the patch size reduces in a dyadic scale that ensures converging to the actual boundary within $log_2(w)$ iterations. It is illustrated graphically in Figure 7.

Figure 7.(a) represents an 8×8 ($w = 8$) patch connected to C_0 that resulted after the ULSCF. Initially, the whole patch represents a boundary patch. Its actual boundary is somewhere within thin patch. Assume the curve made by the connected blue-colored pixels represent the actual boundary as shown in Figure 7.(a)-(d). In the first iteration, the 8 × 8 patch is divided into four 4 × 4 patches. If any 4 × 4 patch does not satisfy the threshold condition, it is marked gray as shown in Figure 7.(b). This step is repeated for the patch size of 2 × 2, and corresponding result is shown in Figure 7.(c). Figure 7.(d) is the last step with $w = 1$.

It is observed that after $log_2(8) = 3$ iterations, the boundary matches exactly with the actual boundary. The improvement of the boundary shape can also be seen on an ultrasound breast tumor image shown in Figure 8. Figure 8.(a) shows a breast tumor, and Figure 8.(b) shows the ground truth boundary as provided in the database [37]. Figure 8.(c) shows the boundary after the ULSCF. In Figure 8.(d-g), boundaries are reproduced for $w = 8, 4, 2$ and 1 respectively. These results clearly show that this step increases smoothness of the boundary with decreasing in w.

E. CONTOUR SMOOTHING

BLSCF increases the accuracy of the segmented region by adopting a logarithmically controlled patch size. The ϕ values of the inside and outside regions are 1 and -1 respectively. We define a boundary contour as a one-pixel-wide curve

along the inside region. Both ULSCF and BLSCF adopt patch-based averaging of intensity that reduces the effect of speckle. The patch size is gradually reduced during BLSCF, and thus the effect of speckle can be seen in the boundary of the segmented region. It suffers from irregularity in shapes due to slope and curvature discontinuities. The smoothness of the boundary is an important requirement satisfied by other level-set based segmentation methods like AC and ACWE. These methods use the length and the curvature of the level-set curve as the regularization terms in the energy function, which ensures the smoothness of the boundary. In this work, a cubic -B spline based contour correction approach was applied, which was earlier used in our earlier work [56]. This step approximates the noisy boundary curve to a regular shaped B-spline curve. It requires 2 threshold parameters which were kept same like our earlier work. The detailed description of this step can be found in [56].

III. RESULTS AND DISCUSSION

The proposed method is developed for the segmentation of all three types of echogenic regions of BUS images from the BITE and the RESECT datasets. In BUS images, HE and anechoic regions are clinically important and the segmentation of these regions is rigorously evaluated for various level-set based methods including the proposed method. In this work, two anechoic regions, namely ventricles and RC and three HE regions LF, CP, tumors were attempted for segmentation. To the best of our knowledge, no annotated dataset is available for BUS image segmentation. Our experiment has been carried out over 1000 different BUS images containing anatomical regions like LF, CP, RC, ventricles, and tumors. The results were subjectively verified by the radiologist and the proposed method is found to be efficient in segmenting all the said regions. In all cases, the proposed method resulted closer to the ground truth and took less time to complete all steps compared to other level-set based methods. Both the BITE and the RESECT datasets contain pre-operative and intra-operative 3D US image stacks for brain tumor patients. With the coordination of the radiologists, we have selectively chosen frames of pBUS and iBUS images from those image stacks where the desired regions are available. For the quantitative evaluation, we prepared a total of 192 and 72 different ground truth BUS image sections from the BITE [10] and the RESECT [58] datasets respectively. Images were prepared using an open-source MATLAB tool *imageAnnotationBOT* [60] in coordination with the third author who is an expert radiologist with an experience of over 15 years in this field. Images with better visibility of regions were chosen for preparing the ground truth images.

For performance comparison, six different level-set based approaches, namely GAC [14], ACWE [17], DRLSE [20], the method of Shi-Karl [19], WLSE [57] and the method by Liu et al. [61] were chosen. For generating the output of brain image segmentation with GAC, ACWE and the DRLSE, an open-source software CREASEG [62] developed on MATLAB was used. The implementation of the methods

TABLE 1. Quality metrics for region-based segmentation.

Metric	Formula
Precision	$\frac{\|S_R \cap S_{GT}\|}{\|S_R \cup S_{GT}\|}$
Sensitivity	$TN = \frac{\|(S_R \cap S_{GT})^c\|}{\|S_{GT}\|}, TP = \left(\frac{\|S_R \cap S_{GT}\|}{\|S_{GT}\|^c}\right)$
Accuracy	$\frac{TP+TN}{TP+FP+TN+FN}$
Dice similarity	$D = \frac{2\|S_R \cap S_{GT}\|}{\|S_R\|+\|S_{GT}\|}$

by Liu et al. [61] and WLSE [57] were done by the authors and used as the state-of-the-art methods for US image segmentation. The results have been presented both graphically and parametrically in terms of region-based quality metrics *accuracy, precision, Dice* and the edge based metrics *asymmetric squared contour distance* (ASCD), and the *root mean squared contour distance* (RMSCD) [63].

Let S_R, S_{GT} respectively be the resulting segmentation and ground truth and $|.|$ signifies their number of pixels within a region. The formulation of the above performance metrics is shown in Table 1.

ASCD and RMSCD measure the dissimilarity between two closed contours. Let E_R and E_{GT} respectively be the closed boundaries of S_R and S_{GT}. The ASCD between S_R and S_{GT} can be expressed as

$$ASCD(S_R, S_{GT})$$
$$= \frac{1}{|E_R| + |E_{GT}|}$$
$$\times \left(\sum_{e_R \in E_R} d_E(e_R, E_{GT}) + \sum_{e_{GT} \in E_{GT}} d_E(e_{GT}, E_R) \right) \quad (15)$$

where $|E_{GT}|$ defines the length of the contour E_{GT}. $d_E(e_{GT}, E_R)$ is the shortest Euclidean distance between a point e_{GT} and E_R is expressed as,

$$d_E(e_{GT}, E_R) = min_{e_R \in E_R} \|e_{GT} - e_R\|_2$$

. $d_E(e_R, E_{GT})$ is defined similarly.

The RMSCD between S_R and S_{GT} can be expressed as,

$$RMSCD(S_R, S_{GT})$$
$$= \sqrt{\frac{1}{|E_R| + |E_{GT}|}}$$
$$\times \sqrt{\left(\sum_{e_R \in E_R} d_E^2(e_R, E_{GT}) + \sum_{e_{GT} \in E_{GT}} d_E^2(e_{GT}, E_R) \right)} \quad (16)$$

The results for the five different regions LF, CP, tumor, *ventricles*, and RC, are shown in Table 2, Table 3, Table 4,, Table 5, and table 6 respectively. Table 2 shows that for the LF segmentation, the proposed method outperforms almost all other methods. The lower the value of ASCD and RMSCD, the better is the performance. The proposed method produced a mean ASCD of 11.177 pixels which was those for the second best results of 11.803 pixels obtained by Liu et al.. Similarly the mean precision, accuracy, and
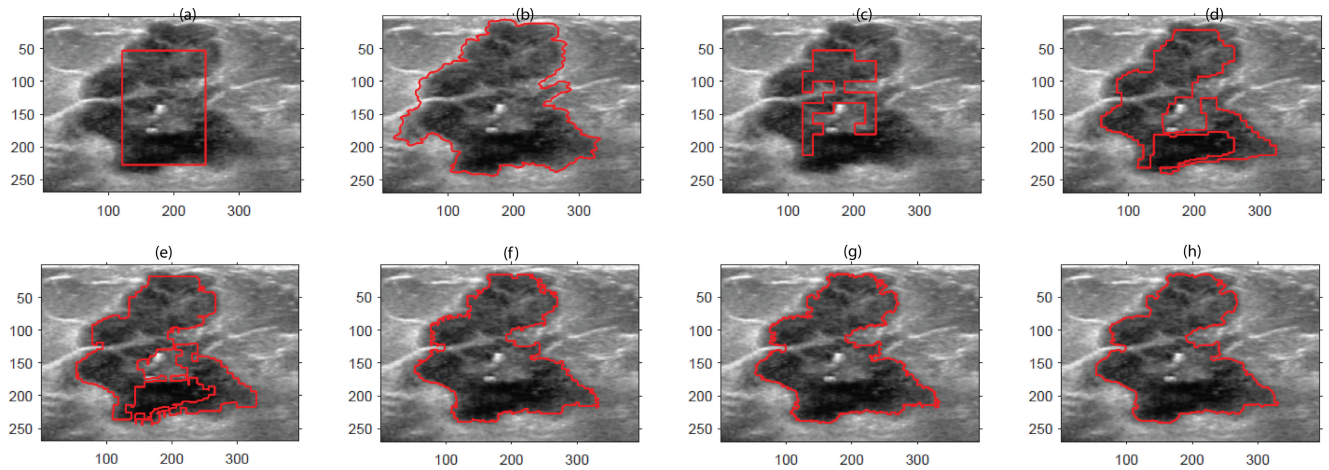
FIGURE 8. (a) Original image with initial boundary selected by the user (b) Ground truth labeled boundary provided in the dataset.(c) Resulting boundaries after unidirectional curve flow (d) Resulting boundary after boundary correction with $w = 8$ (e) Resulting boundary after boundary correction with $w = 4$ (f) Resulting boundary after boundary correction with $w = 2$ (g) Resulting boundary after boundary correction with $w = 1$ (h) Final contour after B-spline curve smoothing.

TABLE 2. Performance comparison of different methods for the segmentation of LF.

Method	Parameters	Precision	Accuracy	Dice	ASCD	RMSCD
GAC	Mean	0.365	0.551	0.525	16.178	26.372
ACWE	Mean	0.39	**0.762**	0.538	21.886	37.562
DRLSE	Mean	0.398	0.567	0.558	21.282	51.406
Shi-Karl's method	Mean	0.353	0.754	0.496	26.599	50.209
WLSE	Mean	0.367	0.59	0.599	20.228	48.406
Method by Liu *et al.*	Mean	0.416	0.605	0.568	11.803	18.035
Method by Nitsch *et al.*	Mean	0.396	0.728	0.599	18.127	22.327
Proposed Method	Mean	**0.496**	0.708	**0.649**	**11.177**	**19.897**

TABLE 3. Comparison of the different methods for segmentation of CP.

Method	Parameters	Precision	Accuracy	Dice	ASCD	RMSCD
GAC	Mean	0.355	0.470	0.496	22.664	33.198
ACWE	Mean	0.653	**0.789**	0.783	8.428	14.492
DRLSE	Mean	0.409	0.661	0.565	24.186	64.164
Shi-Karl's method	Mean	0.409	0.661	0.565	24.186	64.164
WLSE	Mean	0.517	0.774	0.707	22.970	61.503
Method by Liu *et al.*	Mean	0.393	0.493	0.545	11.710	20.507
Method by Nitsch *et al.*	Mean	0.608	0.652	**0.848**	8.681	14.263
Proposed Method	Mean	**0.717**	0.709	0.765	**5.937**	**9.685**

Dice values resulted by the proposed method are 0.496, 0.708, 0.649 which are better than all other methods.

Table 3 shows that the proposed method segments CP better than the other methods and results the mean precision, accuracy, Dice, ASCD and RMSCD of 0.717, 0.709, 0.765, 5.937 and 9.685 pixels respectively. The second best method ACWE results the corresponding values as 0.653, 0.789, 0.783, 8.428 and 14.492 respectively. For a few images, ACWE performed better compared to the proposed method. The proximity of these boundaries with the ground truth is shown by the ASCD and RMSCD values.

The proposed method also resulted better segmentation of the tumor regions as shown in Table 4. It produced the mean ASCD and RMSCD of 9.166 and 13.152 pixels where as, the second best performing method ACWE resulted those

parameters as 13.166 and 19.152 pixels respectively. It was found that the accuracy of 0.847, produced by ACWE was slightly higher than the accuracy of 0.813 as produced by the proposed method.

The proposed method is equally efficient in the segmenting the anechoic regions like ventricles and *RC* as shown in Tables 5 and 6 respectively. It is seen that the accuracy of the proposed method for ventricle segmentation is 0.608 and that for the RC is 0.670. Similarly, the ASCD and RMSCD for the ventricle segmentation resulted in 8.681 and 14.263 pixels respectively against the corresponding second-best performance 8.925 and 17.513 of ACWE. Similar results can be observed in Table 6 where the best mean ASCD and RMSCD obtained by the proposed method were 5.568 and 11.930 pixels where as the second best method ACWE

TABLE 4. Comparison of the different methods for the segmentation of the brain tumor.

Method	Parameters	Precision	Accuracy	Dice	ASCD	RMSCD
GAC	Mean	0.437	0.741	0.571	26.153	37.510
ACWE	Mean	0.585	**0.906**	0.717	13.166	19.152
DRLSE	Mean	0.362	0.640	0.511	34.181	63.831
Shi-Karl's method	Mean	0.493	0.885	0.644	27.126	53.627
WLSE	Mean	0.579	0.901	0.733	25.119	50.884
Method by Liu *et al.*	Mean	0.510	0.847	0.661	21.088	29.865
Method by Nitsch *et al.*	Mean	0.571	0.746	0.718	15.361	28.649
Proposed Method	Mean	**0.620**	0.813	**0.753**	9.166	**13.152**

TABLE 5. Comparison of different methods for the segmentation of the ventricles.

Method	Parameters	Precision	Accuracy	Dice	ASCD	RMSCD
GAC	Mean	0.612	0.740	0.773	9.656	21.274
ACWE	Mean	**0.653**	0.682	0.769	8.925	17.513
DRLSE	Mean	0.436	0.578	0.593	22.348	58.318
Shi-Karl's method	Mean	0.622	0.675	0.735	13.248	48.488
WLSE	Mean	0.485	0.634	0.653	23.993	59.947
Method by Liu *et al.*	Mean	0.473	0.541	0.591	16.829	24.46
Method by Nitsch *et al.*	Mean	0.620	0.813	0.753	13.166	23.152
Proposed Method	Mean	0.638	**0.852**	**0.848**	8.681	**14.263**

TABLE 6. Comparison of different methods for the segmentation of the RC.

Method	Parameters	Precision	Accuracy	Dice	ASCD	RMSCD
GAC	Mean	0.672	0.740	0.773	10.656	21.274
ACWE	Mean	0.653	0.712	0.769	8.125	18.533
DRLSE	Mean	0.436	0.578	0.593	22.348	58.318
Shi-Karl's method	Mean	0.622	0.675	0.735	13.248	48.488
WLSE	Mean	0.490	0.621	0.649	23.908	59.580
Method by Liu *et al.*	Mean	0.473	0.541	0.591	16.829	24.460
Method by Nitsch *et al.*	Mean	0.758	0.765	0.718	7.015	14.597
Proposed Method	Mean	**0.770**	**0.765**	**0.796**	5.568	**11.930**

resulted in 8.125 and 18.533 pixels respectively. Among the region-based metrics, the Dice appears more reliable than the other metrics, and its values match the visually observed assessment. Compared to the region-based metrics, the edge metrics ASCD and RMSCD capture the dissimilarity and compare the segments more accurately. The tables show that the proposed method perform better for all cases in terms of ASCD and RMSCD.

It outperforms other level-set based methods. The visual performance of the proposed algorithm in segmenting LF, CP, tumor, ventricle, and RC is shown in Figure 9, Figure 10, Figure 11, Figure 12, and Figure 13 respectively. In each of these figures (a) shows the targeted section along with the initial rectangular regions marked red, (b) shows the ground truth, (c) - (g) are the outputs of all the competing methods, and (h) shows the segmented boundary resulted by the proposed method. The results demonstrate the superior performance of the proposed method.

The proposed method was applied for the segmentation of anechoic and hypo-echoic regions of breast ultrasound images. The images were collected from the Thammasat university (TU) dataset [37]. Among the three databases of US images, the TU database that contains 300 segmented boundaries of breast tumors. The breast tumor region in the US images is either hypo-echoic or anechoic. The

segmentation performance can be visually compared in Figure 14-16. For almost all the images, the proposed method outperformed other methods and resulted in boundaries closer to the ground truths. GAC can not track the boundaries of the tumors. ACWE also performs well for both HE and anechoic regions but fails for some hypo-echoic regions and regions without strong boundaries.

Recently DL and ML are becoming popular for image segmentation. ML-based approaches require large datasets for training. To the best of our knowledge, there is no annotated dataset for the segmentation various regions of the BUS images. Nitsch et al. [24] performed a ML-based work for classification of the BUS images using training with a limited dataset. They [24] implemented a random forest based BUS image segmentation method on the RESECT dataset, which is capable of training with less number of images. This paper focused on the segmentation of HE regions like falx Cerebri and tentorium cerebelli as a pre-work for the registration of intra-operative US to the pre-operative MR images. US image slices are prepossessed with two stick filters as described in [64]. The stick filters strengthen and sustain the line-type structures and perform smoothing of the homogeneous regions by reducing speckle. After stick filtering, the entire image is divided into *simple linear iterative clustering* (SLIC) superpixels as described in [65].
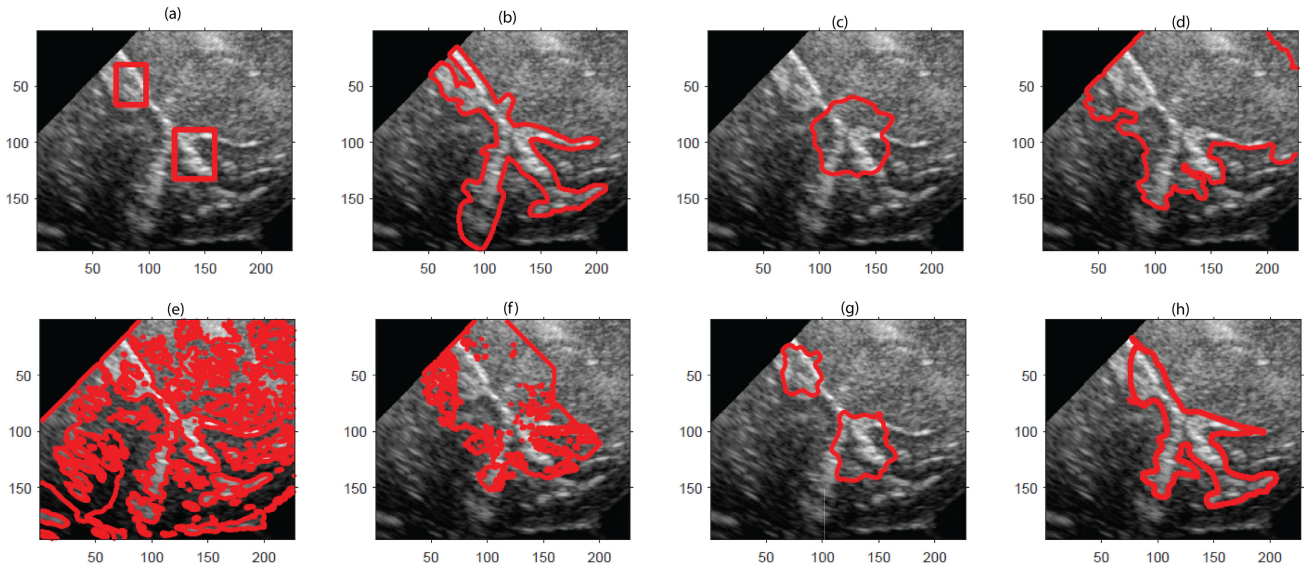
FIGURE 9. (a) Original image with initial boundary selected by the user (b) manually segmented ground truth LF prepared in cooperation with radiologist. Resulting boundaries obtained by GAC is shown in (c), by ACWE is shown in (d), by the method of Shi et al. in (e), by the method of Liu et al. in (f), by WLSE in (g), and the result obtained by the proposed method is shown in (h).
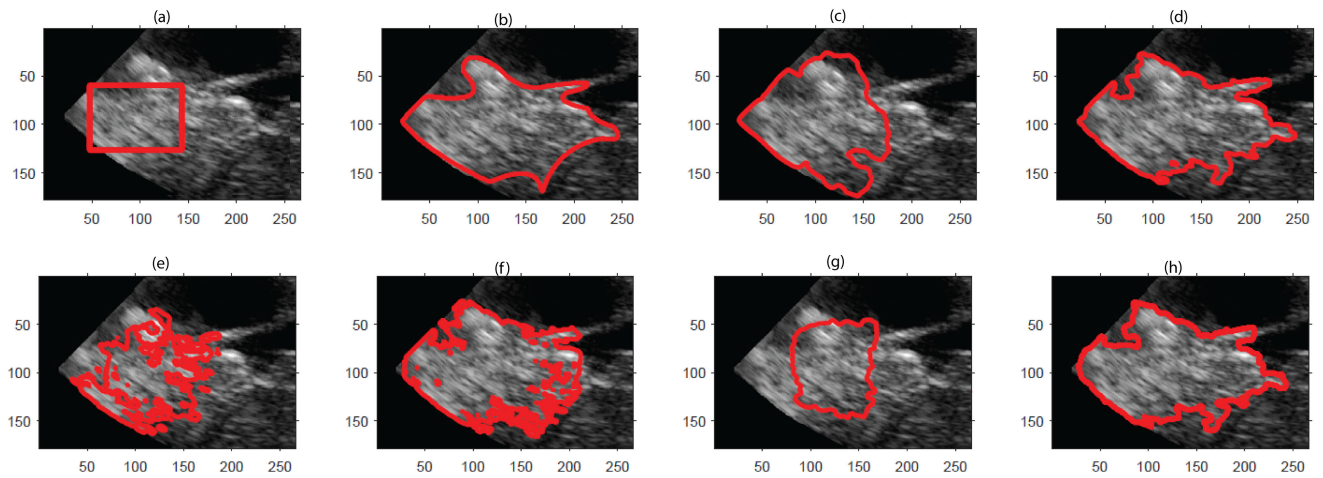

FIGURE 10. (a) Original BUS image with initial boundary selected by the user (b) manually segmented ground truth CP prepared in cooperation with radiologist. Resulting boundaries obtained by GAC is shown in (c), by ACWE is shown in (d), by the method of Shi et al. in (e), by the method of Liu et al. in (f), by WLSE in (g), and the result obtained by the proposed method is shown in (h).

Initially each superpixel is classified by a trained random forest classifier which assigns each normalized super-pixel (λ_i) between 0 and 1 for belonging to a particular class or not. For obtaining the segmented regions, super-pixels are concatenated based on their scores. Superpixels having $\lambda \geq 0.59$, are included in the segmented region. After this step, these neighboring superpixels of the side region having rank values $0.45 \leq \lambda_i \leq 0.59$ are added to the segmented region. Similarly, an additional step is followed where the neighboring superpixels having $0.45 > \lambda_i \geq 0.3$ are also included to the inside region. Figure 17 compares the performance of the random forest based method and the proposed method. The initial rectangular region marked by the user is shown as dotted boundaries in

sub-figures (a1-a3). Figure 17.(b1-b3) show a maroon coloured center region which resulted from the first threshold comparison. Similarly, after the second threshold comparison, the orange colored super-pixels get added to the segmented region. In the third threshold comparison step, the green super-pixels are added and the combined region represents the final results. In Figure 17 (c1-c3), the green coloured boundaries represent the ground truth. The red coloured boundaries are the results produced by the proposed method and the blue colored boundaries are the output of the random forest method. During the implementation of the method by Nitsch et al., we have considered five classes (LF, CP, tumor, ventricle, and RC). A total of 192 image sections were chosen and out of these, 166 images were used for
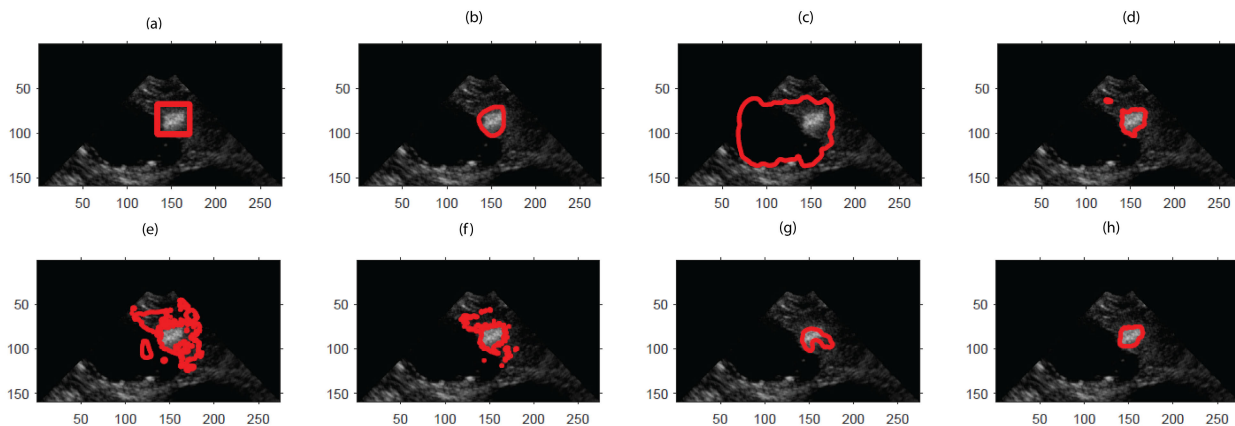
FIGURE 11. (a) Original BUS image with initial boundary selected by the user (b) manually segmented ground truth *tumor* prepared in cooperation with radiologist. Resulting boundaries obtained by GAC is shown in (c), by ACWE is shown in (d), by the method of Shi et al. in (e), by the method of Liu et al. in (f), by WLSE in (g), and the result obtained by the proposed method is shown in (h).
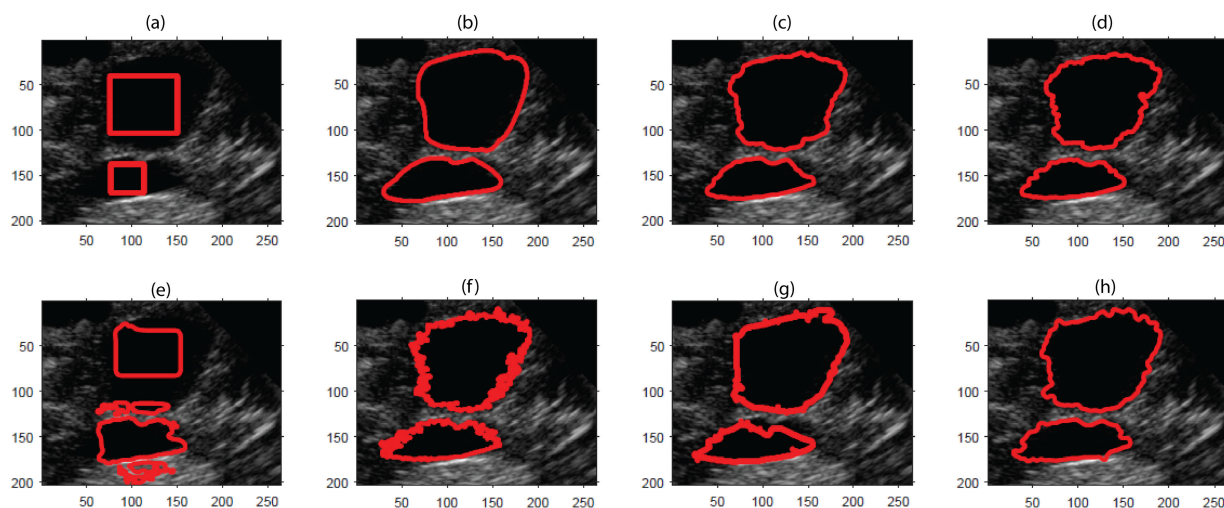

FIGURE 12. (a) Original BUS image with initial boundary selected by the user (b) manually segmented ground truth ventricles prepared in cooperation with radiologist. Resulting boundaries obtained by GAC is shown in (c), by ACWE is shown in (d), by the method of Shi et al. in (e), by the method of Liu et al. in (f), by WLSE in (g) and the result obtained by the proposed method is shown in (h).
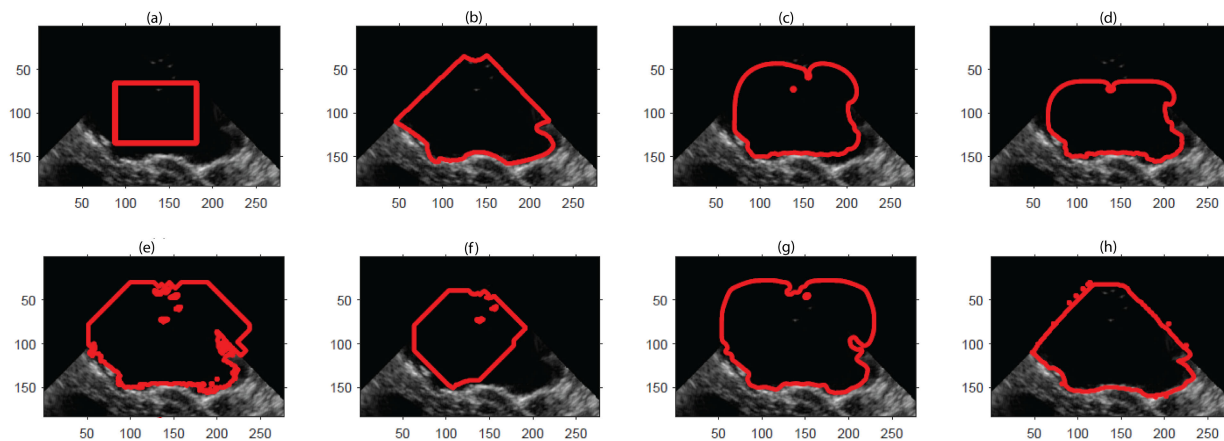

FIGURE 13. (a) Original BUS image with initial boundary selected by the user (b) manually segmented ground truth ventricles prepared in cooperation with radiologist. Resulting boundaries obtained by GAC is shown in (c), by ACWE is shown in (d), by the method of Shi et al. in (e), by the method of Liu et al. in (f), by WLSE in (g) and the result obtained by the proposed method is shown in (h).
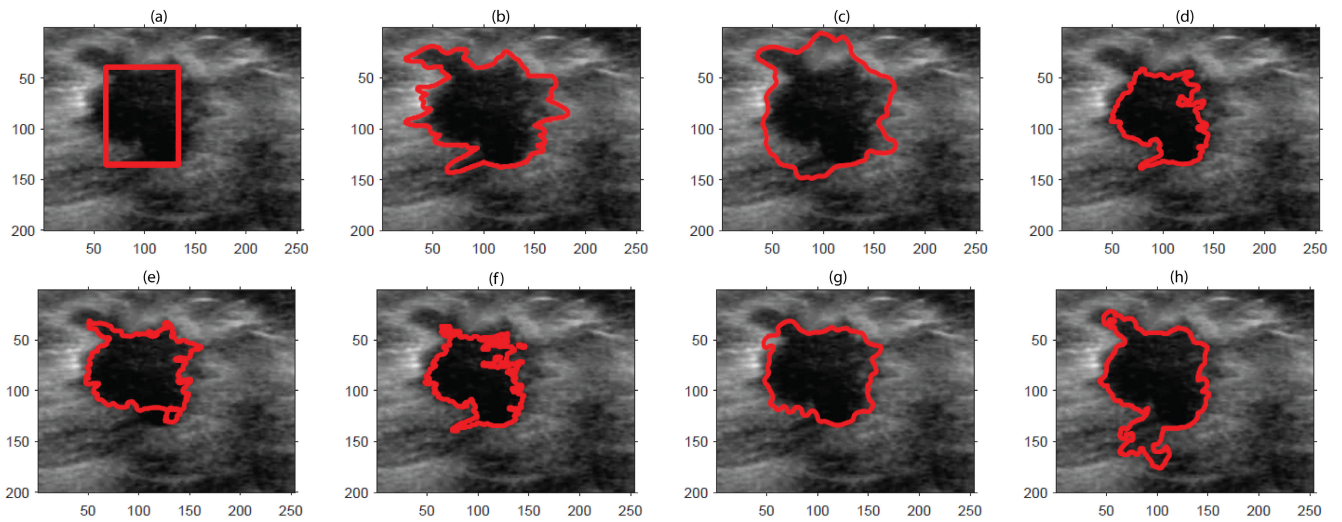
FIGURE 14. (a) Original BUS image with initial boundary selected by the user (b) Ground truth labeled boundary provided in the dataset. Resulting boundaries obtained by GAC is shown in (c), result by ACWE is shown in (d), result by the method of Shi et al. is shown in (e), result by the method of Liu et al. is shown in (f), by WLSE in (g) and the result obtained by the proposed method is shown in (h).
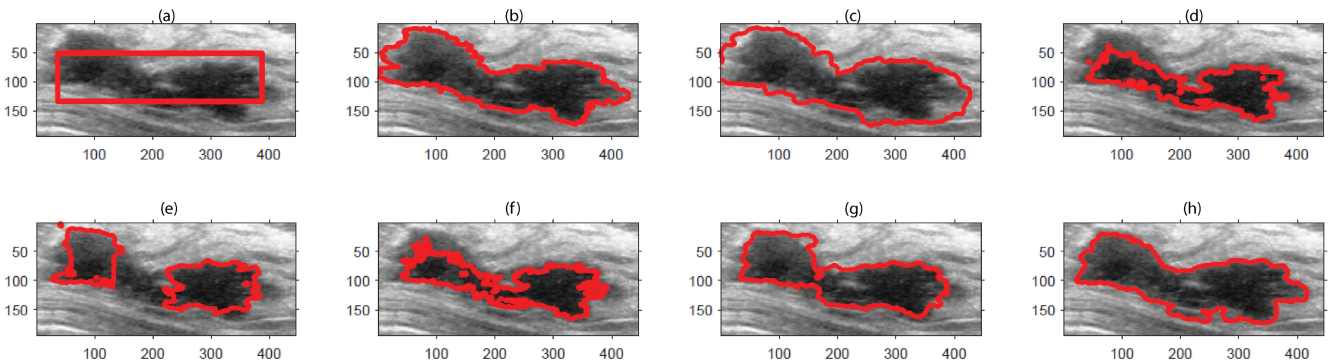

FIGURE 15. (a) Original brest US image with initial boundary selected by the user, (b) Ground truth labeled boundary provided in the dataset. Resulting boundaries obtained by GAC is shown in (c), by ACWE is shown in (d), by the method of Shi et al. is shown in (e), by the method of Liu et al. is shown in (f), by WLSE in (g) and by the proposed method is shown in (h).

FIGURE 16. (a) Original image with initial boundary selected by the user (b) Ground truth labeled boundary provided in the dataset. Resulting boundaries obtained by GAC is shown in (c), by ACWE is shown in (d), by the method of Shi.et al. is shown in (e), by the method of Liu et al. is shown in (f), by WLSE in (g) and by the proposed method is shown in (h).
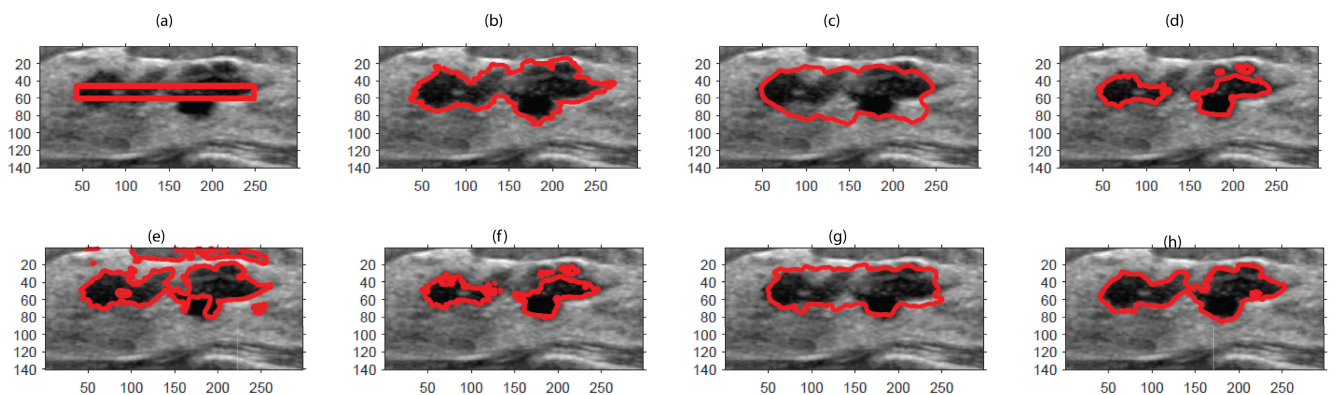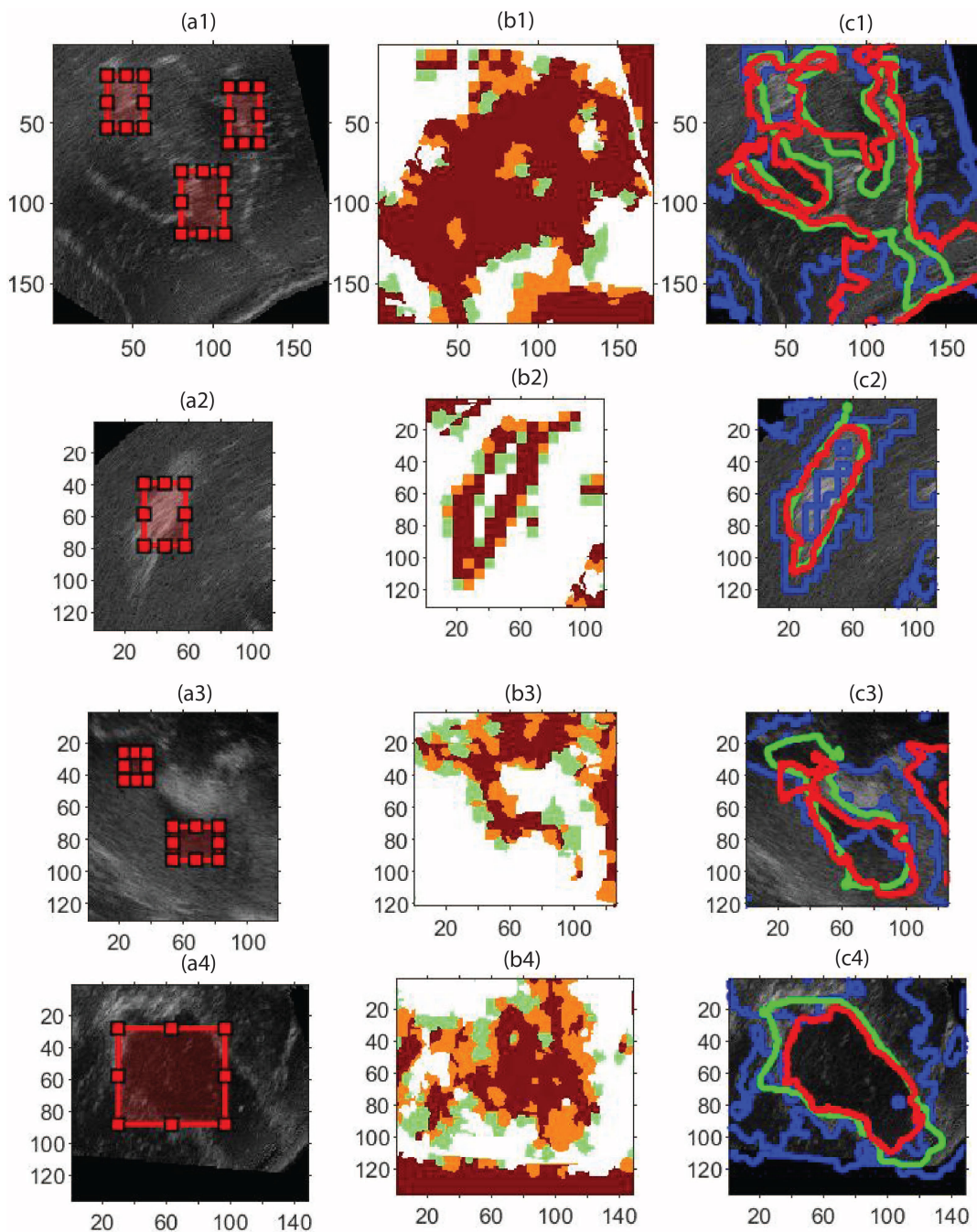
FIGURE 17. (a1-a4) and corresponding row represent the original BUS image section of LF, CP ventricles and RC respectively and their results. The dotted red coloured boundaries in (a1-a4) represent the initial region marked by the user. The maroon coloured regions in (b1-b4) are the group of superpixels having ($\lambda_i \geq 0.59$). Similarly the orange coloured superpixels are neighbouring to the maroon region and have $0.59 > \lambda_i \geq 0.45$. The green coloured superpixels are neighbouring to the combined maroon and orange region resulted after the second thresholding and have $0.45 \geq \lambda_i > 0.3$. The green coloured boundaries in the figures (c1-c4) are the ground truths of the Figure (a1-a4) respectively. The red coloured boundaries are results of the proposed methods and the blue coloured boundaries are resulted by the method of Nitsch et al.

training and 26 images were kept for testing. The training and testing images are a rectangular areas in the ROI in the database images. The quantitative evaluation for the method by Nitsch et al. was done only on 26 images whereas for other methods, a total of 168 images were used for evaluations. Quantitative evaluation for all different regions are shown in Tables 2- 6. Figure 17 show that the performance of the proposed method is comparatively better, because it produces boundaries close to the actual boundaries but in most cases. The results produced by the random forest method may get improved if the number of training images is increased.
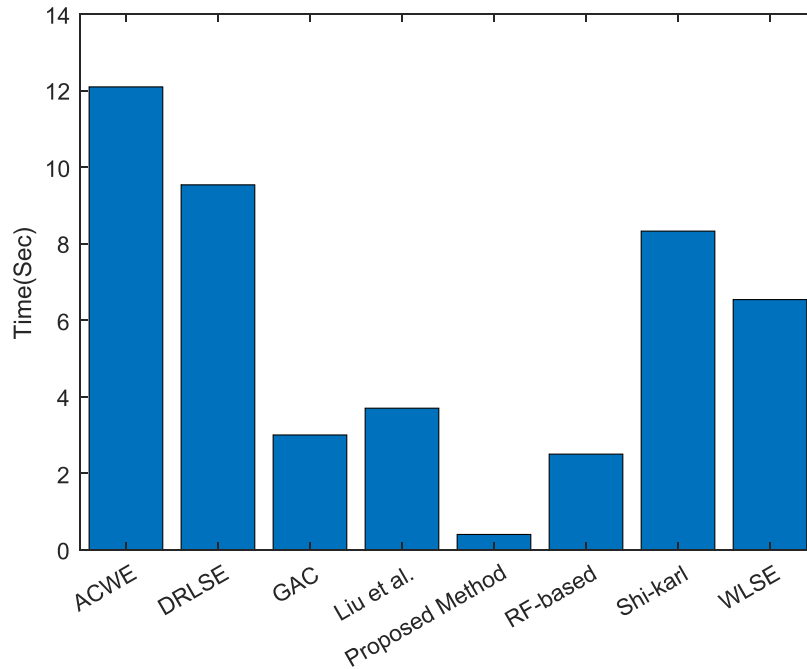
Apart from the better segmentation performance, the proposed method is computationally faster compared to the other methods. The methods such as GAC [14], ACWE [17], DRLSE [20], and WLSE [57] estimate and minimize of the energy function which is computationally expensive. The ML-based method of Nitsch et al. [24] requires partitioning the image into superpixels, which is computationally expensive. In addition to that, various rule-based concatenation of the superpixels requires additional computations. For comparing the speed of the convergence of the said algorithms, experiments were conducted in the same computer loaded with MATLAB, and having a ninth-generation Intel Core-i5 processor (2.40 GHz) and 16 GB DDR4 RAM. We recorded the times it takes for the various steps of the proposed methods and the time taken by other algorithms with the best possible parameter setups. The comparative results shown in Figure 18 show that the proposed method takes average time of 0.48 sec which is about 20-50 times faster than other methods. The bar diagrams in FIGURE 18 show the average time of segmentation of all 192 image sections used for the parametric study. The time taken by the method of Nitsch et al. is only due to the classification and rule-based concatenation of the superpixels. From this comparative study, it is evident that the proposed method is faster compared to other methods and has the potential for being used as an assisting tool to the neurosurgeon during brain surgery.

Though the proposed work performs better compared to the other approaches, it has a few limitations which are listed below.

1) When multiple regions are connected in a BUS image due to any artifact of similar intensity profile, they can not be separated, and manual segmentation is required.

2) Sometimes the coefficients of μ_R and σ_R in Equations (8), (9), and (10) are needed to be varied because of surrounding image regions, but in most cases, it provides good results.

3) During ground truth preparation, boundaries of the different regions were verified by one radiologist only. The involvement of a neurosurgeon in this work will be more appropriate.

This work could not be compared with any DL-based segmentation methods because of the non-availability of sufficient data. It can be done in the near future as an extension of this article.

IV. CONCLUSION

The paper introduced a patch-based level-set curve evolution method which efficiently segments various regions in US images based on their echogenicity. Depending on the type of region to be segmented, an upper and a lower thresholds are estimated from the initial rectangular region chosen by the user. The segmentation method combines a patch-based unidirectional curve flow followed by a bi-directional boundary correction. The unidirectional level-set step grossly segments the desired region and produces approximate and blocky boundaries. The bidirectional level-set curve flow continues for limited number of iterations and it works only on the boundary region with patch sizes reducing at a dyadic scale in every iteration. This step starts with a patch size of 8 and until patch size reduces to 1. Further smoothness of the boundary is obtained by a curvature controlled cubic B-spline interpolation method. Results have been compared with other level-set based methods and a super-pixel based

random forest classifier. Graphical and quantitative results show that the proposed method outperforms other level-set based methods and the random-forest classifier. This is fast compared to other methods because of its patch-based processing and boundaries do not suffer from slope and curvature discontinuities. This method can be used as an assistive tool for BUS image segmentation prior to BUS image registration.

REFERENCES

[1] V. Rajinikanth, N. Dey, R. Kumar, J. Panneerselvam, and N. S. M. Raja, "Fetal head periphery extraction from ultrasound image using Jaya algorithm and Chan-Vese segmentation," *Procedia Comput. Sci.*, vol. 152, pp. 66–73, 2019.

[2] J. Yu, Y. Wang, P. Chen, and Y. Shen, "Fetal abdominal contour extraction and measurement in ultrasound images," *Ultrasound Med. Biol.*, vol. 34, no. 2, pp. 169–182, Feb. 2008.

[3] R. M. Rad, P. Saeedi, J. Au, and J. Havelock, "Trophectoderm segmentation in human embryo images via inceptioned U-Net," *Med. Image Anal.*, vol. 62, May 2020, Art. no. 101612.

[4] S. Ghose, A. Oliver, J. Mitra, R. Martí, X. Lladó, J. Freixenet, D. Sidibé, J. C. Vilanova, J. Comet, and F. Meriaudeau, "A supervised learning framework of statistical shape and probability priors for automatic prostate segmentation in ultrasound images," *Med. Image Anal.*, vol. 17, no. 6, pp. 587–600, Aug. 2013.

[5] H. R. Torres, S. Queirós, P. Morais, B. Oliveira, J. C. Fonseca, and J. L. Vilaça, "Kidney segmentation in ultrasound, magnetic resonance and computed tomography images: A systematic review," *Comput. Methods Programs Biomed.*, vol. 157, pp. 49–67, Apr. 2018.

[6] D. Mishra, S. Chaudhury, M. Sarkar, and A. S. Soin, "Ultrasound image segmentation: A deeply supervised network with attention to boundaries," *IEEE Trans. Biomed. Eng.*, vol. 66, no. 6, pp. 1637–1648, Jun. 2019.

[7] L. Ma, H. Kiyomatsu, K. Nakagawa, J. Wang, E. Kobayashi, and I. Sakuma, "Accurate vessel segmentation in ultrasound images using a local-phase-based snake," *Biomed. Signal Process. Control*, vol. 43, pp. 236–243, May 2018.

[8] X. Liu, D. Zhang, J. Yao, and J. Tang, "Transformer and convolutional based dual branch network for retinal vessel segmentation in OCTA images," *Biomed. Signal Process. Control*, vol. 83, May 2023, Art. no. 104604.

[9] L. Mercier, R. F. Del Maestro, K. Petrecca, A. Kochanowska, S. Drouin, C. X. B. Yan, A. L. Janke, S. J.-S. Chen, and D. L. Collins, "New prototype neuronavigation system based on preoperative imaging and intraoperative freehand ultrasound: System description and validation," *Int. J. Comput. Assist. Radiol. Surgery*, vol. 6, no. 4, pp. 507–522, Jul. 2011.

[10] L. Mercier, R. F. Del Maestro, K. Petrecca, D. Araujo, C. Haegelen, and D. L. Collins, "Online database of clinical MR and ultrasound images of brain tumors," *Med. Phys.*, vol. 39, no. 6, pp. 3253–3261, Jun. 2012.

[11] R. C. Gonzalez and R. E. Woods, *Digital Image Processing*. London, U.K.: Pearson Education, 2002.

[12] G. Xiao, M. Brady, J. A. Noble, and Y. Zhang, "Segmentation of ultrasound B-mode images with intensity inhomogeneity correction," *IEEE Trans. Med. Imag.*, vol. 21, no. 1, pp. 48–57, 2002.

[13] Y.-L. Huang and D.-R. Chen, "Watershed segmentation for breast tumor in 2-D sonography," *Ultrasound Med. Biol.*, vol. 30, no. 5, pp. 625–632, May 2004.

[14] V. Caselles, R. Kimmel, and G. Sapiro, "Geodesic active contours," *Int. J. Comput. Vis.*, vol. 22, no. 1, pp. 61–79, 1997.

[15] A. Faisal, S.-C. Ng, and K. W. Lai, "Multiple active contours using scalable local regional information on expandable kernel," in *Proc. IEEE Conf. Biomed. Eng. Sci. (IECBES)*, Dec. 2014, pp. 541–544.

[16] A. Faisal, S.-C. Ng, S.-L. Goh, J. George, E. Supriyanto, and K. W. Lai, "Multiple LREK active contours for knee meniscus ultrasound image segmentation," *IEEE Trans. Med. Imag.*, vol. 34, no. 10, pp. 2162–2171, Oct. 2015.

[17] T. F. Chan and L. A. Vese, "Active contours without edges," *IEEE Trans. Image Process.*, vol. 10, no. 2, pp. 266–277, Oct. 2001.

[18] O. Bernard, D. Friboulet, P. Thevenaz, and M. Unser, "Variational B-spline level-set: A linear filtering approach for fast deformable model evolution," *IEEE Trans. Image Process.*, vol. 18, no. 6, pp. 1179–1191, Jun. 2009.

[19] Y. Shi and W. C. Karl, "A real-time algorithm for the approximation of level-set-based curve evolution," *IEEE Trans. Image Process.*, vol. 17, no. 5, pp. 645–656, May 2008.

[20] C. Li, C. Xu, C. Gui, and M. D. Fox, "Distance regularized level set evolution and its application to image segmentation," *IEEE Trans. Image Process.*, vol. 19, no. 12, pp. 3243–3254, Dec. 2010.

[21] C. Keatmanee, U. Chaumrattanakul, K. Kotani, and S. S. Makhanov, "Initialization of active contours for segmentation of breast cancer via fusion of ultrasound, Doppler, and elasticity images," *Ultrasonics*, vol. 94, pp. 438–453, Apr. 2019.

[22] H.-M. Wu and H. H.-S. Lu, "Iterative sliced inverse regression for segmentation of ultrasound and MR images," *Pattern Recognit.*, vol. 40, no. 12, pp. 3492–3502, Dec. 2007.

[23] Y. Zhan and D. Shen, "Deformable segmentation of 3-D ultrasound prostate images using statistical texture matching method," *IEEE Trans. Med. Imag.*, vol. 25, no. 3, pp. 256–272, Mar. 2006.

[24] J. Nitsch, J. Klein, P. Dammann, K. Wrede, O. Gembruch, J. H. Moltz, H. Meine, U. Sure, R. Kikinis, and D. Miller, "Automatic and efficient MRI-US segmentations for improving intraoperative image fusion in image-guided neurosurgery," *NeuroImage, Clin.*, vol. 22, Oct. 2019, Art. no. 101766.

[25] W.-X. Liao, P. He, J. Hao, X.-Y. Wang, R.-L. Yang, D. An, and L.-G. Cui, "Automatic identification of breast ultrasound image based on supervised block-based region segmentation algorithm and features combination migration deep learning model," *IEEE J. Biomed. Health Informat.*, vol. 24, no. 4, pp. 984–993, Apr. 2020.

[26] H. Li, J. Fang, S. Liu, X. Liang, X. Yang, Z. Mai, M. T. Van, T. Wang, Z. Chen, and D. Ni, "CR-unet: A composite network for ovary and follicle segmentation in ultrasound images," *IEEE J. Biomed. Health Informat.*, vol. 24, no. 4, pp. 974–983, Apr. 2020.

[27] M. Alkhatib, A. Hafiane, P. Vieyres, and A. Delbos, "Deep visual nerve tracking in ultrasound images," *Computerized Med. Imag. Graph.*, vol. 76, Sep. 2019, Art. no. 101639.

[28] L. Han, Y. Huang, H. Dou, S. Wang, S. Ahamad, H. Luo, Q. Liu, J. Fan, and J. Zhang, "Semi-supervised segmentation of lesion from breast ultrasound images with attentional generative adversarial network," *Comput. Methods Programs Biomed.*, vol. 189, Jun. 2020, Art. no. 105275.

[29] A. Vakanski, M. Xian, and P. E. Freer, "Attention-enriched deep learning model for breast tumor segmentation in ultrasound images," *Ultrasound Med. Biol.*, vol. 46, no. 10, pp. 2819–2833, Oct. 2020.

[30] Y. Xu, Y. Wang, J. Yuan, Q. Cheng, X. Wang, and P. L. Carson, "Medical breast ultrasound image segmentation by machine learning," *Ultrasonics*, vol. 91, pp. 1–9, Jan. 2019.

[31] J. Yang, M. Faraji, and A. Basu, "Robust segmentation of arterial walls in intravascular ultrasound images using dual path U-Net," *Ultrasonics*, vol. 96, pp. 24–33, Jul. 2019.

[32] M. D. M. Vila, B. Remeseiro, M. Grau, R. Elosua, À. Betriu, E. Fernandez-Giraldez, and L. Igual, "Semantic segmentation with DenseNets for carotid artery ultrasound plaque segmentation and CIMT estimation," *Artif. Intell. Med.*, vol. 103, Mar. 2020, Art. no. 101784.

[33] L. Canalini, J. Klein, D. Miller, and R. Kikinis, "Segmentation-based registration of ultrasound volumes for glioma resection in image-guided neurosurgery," *Int. J. Comput. Assist. Radiol. Surgery*, vol. 14, no. 10, pp. 1697–1713, Oct. 2019.

[34] S. Ji, Z. Wu, A. Hartov, D. W. Roberts, and K. D. Paulsen, "Mutual-information-based image to patient re-registration using intraoperative ultrasound in image-guided neurosurgery," *Med. Phys.*, vol. 35, no. 10, pp. 4612–4624, Oct. 2008.

[35] X. Fan, D. W. Roberts, J. D. Olson, S. Ji, T. J. Schaewe, D. A. Simon, and K. D. Paulsen, "Image updating for brain shift compensation during resection," *Operative Neurosurgery*, vol. 14, no. 4, pp. 402–411, 2018.

[36] O. Zvitia, A. Mayer, R. Shadmi, S. Miron, and H. K. Greenspan, "Co-registration of white matter tractographies by adaptive-mean-shift and Gaussian mixture modeling," *IEEE Trans. Med. Imag.*, vol. 29, no. 1, pp. 132–145, Jan. 2010.

[37] A. Boezaart and B. Ihnatsenka, "Ultrasound: Basic understanding and learning the language," *Int. J. Shoulder Surgery*, vol. 4, no. 3, p. 55, 2010.

[38] S. Osher and J. A. Sethian, "Fronts propagating with curvature-dependent speed: Algorithms based on hamilton-jacobi formulations," *J. Comput. Phys.*, vol. 79, no. 1, pp. 12–49, Nov. 1988.

[39] J. A. Sethian, *Level Set Methods and Fast Marching Methods*, vol. 98. Cambridge, U.K.: Cambridge Univ. Press, 1999.

[40] Y. Wang, H. Dou, X. Hu, L. Zhu, X. Yang, M. Xu, J. Qin, P.-A. Heng, T. Wang, and D. Ni, "Deep attentive features for prostate segmentation in 3D transrectal ultrasound," *IEEE Trans. Med. Imag.*, vol. 38, no. 12, pp. 2768–2778, Dec. 2019.

[41] D. Karimi, Q. Zeng, P. Mathur, A. Avinash, S. Mahdavi, I. Spadinger, P. Abolmaesumi, and S. E. Salcudean, "Accurate and robust deep learning-based segmentation of the prostate clinical target volume in ultrasound images," *Med. Image Anal.*, vol. 57, pp. 186–196, Oct. 2019.

[42] S. Zhou, H. Wu, J. Gong, T. Le, H. Wu, Q. Chen, and Z. Xu, "Mark-guided segmentation of ultrasonic thyroid nodules using deep learning," in *Proc. 2nd Int. Symp. Image Comput. Digit. Med.*, Oct. 2018, pp. 21–26.

[43] F. Zhu, Z. Gao, C. Zhao, Z. Zhu, J. Tang, Y. Liu, S. Tang, C. Jiang, X. Li, M. Zhao, and W. Zhou, "Semantic segmentation using deep learning to extract total extraocular muscles and optic nerve from orbital computed tomography images," *Optik*, vol. 244, Oct. 2021, Art. no. 167551.

[44] S. Yin, Q. Peng, H. Li, Z. Zhang, X. You, K. Fischer, S. L. Furth, G. E. Tasian, and Y. Fan, "Automatic kidney segmentation in ultrasound images using subsequent boundary distance regression and pixelwise classification networks," *Med. Image Anal.*, vol. 60, Feb. 2020, Art. no. 101602.

[45] S. Yin, Q. Peng, H. Li, Z. Zhang, X. You, K. Fischer, S. L. Furth, Y. Fan, and G. E. Tasian, "Multi-instance deep learning of ultrasound imaging data for pattern classification of congenital abnormalities of the kidney and urinary tract in children," *Urology*, vol. 142, pp. 183–189, Aug. 2020.

[46] S. Moradi, M. G. Oghli, A. Alizadehasl, I. Shiri, N. Oveisi, M. Oveisi, M. Maleki, and J. Dhooge, "MFP-unet: A novel deep learning based approach for left ventricle segmentation in echocardiography," *Phys. Medica*, vol. 67, pp. 58–69, Nov. 2019.

[47] Y. Hu, B. Xia, M. Mao, Z. Jin, J. Du, L. Guo, A. F. Frangi, B. Lei, and T. Wang, "AIDAN: An attention-guided dual-path network for pediatric echocardiography segmentation," *IEEE Access*, vol. 8, pp. 29176–29187, 2020.

[48] Q. Meng, M. Sinclair, V. Zimmer, B. Hou, M. Rajchl, N. Toussaint, O. Oktay, J. Schlemper, A. Gomez, J. Housden, J. Matthew, D. Rueckert, J. A. Schnabel, and B. Kainz, "Weakly supervised estimation of shadow confidence maps in fetal ultrasound imaging," *IEEE Trans. Med. Imag.*, vol. 38, no. 12, pp. 2755–2767, Dec. 2019.

[49] R. Qu, G. Xu, C. Ding, W. Jia, and M. Sun, "Deep learning-based methodology for recognition of fetal brain standard scan planes in 2D ultrasound images," *IEEE Access*, vol. 8, pp. 44443–44451, 2020.

[50] L. Xu, M. Liu, Z. Shen, H. Wang, X. Liu, X. Wang, S. Wang, T. Li, S. Yu, M. Hou, J. Guo, J. Zhang, and Y. He, "DW-net: A cascaded convolutional neural network for apical four-chamber view segmentation in fetal echocardiography," *Computerized Med. Imag. Graph.*, vol. 80, Mar. 2020, Art. no. 101690.

[51] N. Mu, Z. Lyu, M. Rezaeitaleshmahalleh, J. Tang, and J. Jiang, "An attention residual u-net with differential preprocessing and geometric post-processing: Learning how to segment vasculature including intracranial aneurysms," *Med. Image Anal.*, vol. 84, Feb. 2023, Art. no. 102697.

[52] O. Ronneberger, P. Fischer, and T. Brox, "U-net: Convolutional networks for biomedical image segmentation," in *Proc. Int. Conf. Med. Image Comput. Comput.-Assist. Intervent.* Cham, Switzerland: Springer, 2015, pp. 234–241.

[53] S. Xie, R. Girshick, P. Dollár, Z. Tu, and K. He, "Aggregated residual transformations for deep neural networks," in *Proc. IEEE Conf. Comput. Vis. Pattern Recognit. (CVPR)*, Jul. 2017, pp. 1492–1500.

[54] D. Mahapatra, "Semi-supervised learning and graph cuts for consensus based medical image segmentation," *Pattern Recognit.*, vol. 63, pp. 700–709, Mar. 2017.

[55] Z. Feng, D. Nie, L. Wang, and D. Shen, "Semi-supervised learning for pelvic MR image segmentation based on multi-task residual fully convolutional networks," in *Proc. IEEE 15th Int. Symp. Biomed. Imag. (ISBI)*, Apr. 2018, pp. 885–888.

[56] H. Chel, P. K. Bora, and K. K. Ramchiary, "A fast technique for hyper-echoic region separation from brain ultrasound images using patch based thresholding and cubic B-spline based contour smoothing," *Ultrasonics*, vol. 111, Mar. 2021, Art. no. 106304.

[57] A. Khadidos, V. Sanchez, and C.-T. Li, "Weighted level set evolution based on local edge features for medical image segmentation," *IEEE Trans. Image Process.*, vol. 26, no. 4, pp. 1979–1991, Apr. 2017.

[58] Y. Xiao, M. Fortin, G. Unsgård, H. Rivaz, and I. Reinertsen, "REtro-Spective evaluation of cerebral tumors (RESECT): A clinical database of pre-operative MRI and intra-operative ultrasound in low-grade glioma surgeries," *Med. Phys.*, vol. 44, no. 7, pp. 3875–3882, Jul. 2017.

[59] W. Niblack, *An Introduction to Digital Image Processing*. Denmark, Europe: Strandberg Publishing Company, 1985.

[60] M. Cicconet. *Imageannotationbot*. [Online]. Available: https://www.mathworks.com/matlabcentral/fileexchange/64719-imageannotationbot

[61] B. Liu, H. D. Cheng, J. Huang, J. Tian, X. Tang, and J. Liu, "Probability density difference-based active contour for ultrasound image segmentation," *Pattern Recognit.*, vol. 43, no. 6, pp. 2028–2042, Jun. 2010.

[62] T. Dietenbeck, M. Alessandrini, D. Friboulet, and O. Bernard, "Creaseg: A free software for the evaluation of image segmentation algorithms based on level-set," in *Proc. IEEE Int. Conf. Image Process.*, Sep. 2010, pp. 665–668.

[63] S. Rueda et al., "Evaluation and comparison of current fetal ultrasound image segmentation methods for biometric measurements: A grand challenge," *IEEE Trans. Med. Imag.*, vol. 33, no. 4, pp. 797–813, Apr. 2014.

[64] J. Nitsch, J. Klein, D. Miller, U. Sure, and H. K. Hahn, "Automatic segmentation of the cerebral falx and adjacent gyri in 2D ultrasound images," in *Bildverarbeitung für Die Medizin*. Cham, Switzerland: Springer, 2015, pp. 287–292.

[65] R. Achanta, A. Shaji, K. Smith, A. Lucchi, P. Fua, and S. Süsstrunk, "SLIC superpixels compared to state-of-the-art superpixel methods," *IEEE Trans. Pattern Anal. Mach. Intell.*, vol. 34, no. 11, pp. 2274–2282, Nov. 2012.

HARADHAN CHEL (Member, IEEE) received the M.Tech. degree in communication engineering from the National Institute of Technology Durgapur, India, in 2009. He is currently pursuing the Ph.D. degree with the Department of Electronics and Electrical Engineering, Indian Institute of Technology Guwahati, India. He joined Bharat Sanchar Nigam Ltd., India, as an Executive Engineer, in 2009. Later he shifted into the academic field and joined the Central Institute of Technology Kokrajhar, as an Assistant Professor, in 2012. His research interests include image processing, brain ultrasound image processing, and deep learning for images.

PRABIN KUMAR BORA received the B.Eng. degree in electrical engineering from the Assam Engineering College, Guwahati, India, in 1981, and the M.Eng. and Ph.D. degrees in electrical engineering from the Indian Institute of Science, Bengaluru, in 1988 and 1993, respectively. He was a Faculty Member with the Assam Engineering College, the Jorhat Engineering College, Jorhat, India, and Gauhati University, Guwahati. He is currently a Professor with the Department of Electronics and Electrical Engineering, Indian Institute of Technology Guwahati, India. His research interests include the application of signal processing and ML techniques for images, videos, communication signals, and biomedical signals.

KANDARPA KUMAR RAMCHIARY (Member, IEEE) received the M.B.B.S. degree from the Guwahati Medical College, India, in 1994, and the M.D. degree in radio diagnosis from Dibrugarh University, Assam, India, in 1999. He was a Senior Lecturer with the Regional Institute of Paramedical and Nursing sciences (RIPANS) under the North-East Council, from 1999 to 2006. He has been a Senior Radiologist with the City Clinic and Research Centre, Kokrajhar, Assam, India, since 2006. His research interest includes clinical radiology.

● ● ●